Astron. Astrophys. 342, 717–735 (1999)

ASTRONOMY AND ASTROPHYSICS

Ionization and density along the beams of Herbig-Haro jets

Francesca Bacciotti[1,⋆] **and Jochen Eislöffel**[2,3,4]

[1] Osservatorio Astrofisico di Arcetri, Largo E. Fermi 5, I-50125 Firenze, Italy (e-mail: fran@arcetri.astro.it)
[2] Institute for Astronomy, University of Hawaii, 2680 Woodlawn Drive, Honolulu, HI 96822, USA
[3] Max-Planck-Institut für Astronomie, Königstuhl 17, D-69117 Heidelberg, Germany
[4] Thüringer Landessternwarte Tautenburg, Sternwarte 5, D-07778 Tautenburg, Germany (e-mail: jochen@tls-tautenburg.de)

Received 1 August 1997 / Accepted 29 October 1998

Abstract. Physical properties of several well-known Herbig-Haro jets are investigated using an improved version of the spectroscopic diagnostic technique originally developed by Bacciotti et al. (1995). The procedure allows one to derive in a model-independent way the hydrogen ionization fraction in regions of low excitation. The ionization fraction, the electron and gas density, and the average excitation temperature are derived for various positions along the flows.

We find that the hydrogen ionization fraction, with typical initial values of 20–30%, generally decreases along the whole jet or along parts of the flow, following well-defined recombination laws. These results are consistent with the idea that the gas is initially ionized in the jet acceleration region, and then slowly recombines while traveling away from the source. If shocks along the jet beam are present, they can at most have a minor contribution to the ionization of the gas, as apparent in HH 34 and in the first 45″ of the HH 46/47 jet, where the ionization fraction decreases almost monotonically. In the jets in which re-ionization episodes occur (i.e. HH 24C/E and HH 24G), the ionization fraction suddenly increases and then gently decays *downstream of the re-ionization event*. Both findings apparently disfavour a mini-bow shock interpretation for the production of the ionization of the beam.

The total densities derived from the ratio between the electron density and the ionization fraction range from about 10^3 to a few $10^4\,\mathrm{cm}^{-3}$. Without applying a correction for shock compression, the average mass loss rate varies from $3.8\ 10^{-8}$ (in the HL Tau jet) to $1.2\ 10^{-6}\,\mathrm{M}_\odot\,\mathrm{yr}^{-1}$ (in HH24 G), while momentum supply rates vary between $1.6\ 10^{-5}$ (in the HL Tau jet) and $3.1\ 10^{-4}\,\mathrm{M}_\odot\,\mathrm{yr}^{-1}\,\mathrm{km\,s}^{-1}$ (in HH 24G). Taking shock compression into account, these values may be reduced by a factor 3–5.

Key words: ISM: kinematics and dynamics – ISM: jets and outflows – stars: formation – line: formation

1. Introduction

Bipolar collimated mass flows associated with young stellar objects (YSOs) have widely been recognized as an essential ingredient of the star formation process. Here, we focus on the highly–collimated optical Herbig–Haro (HH) jets (e.g. Eislöffel 1996, Ray 1996). They manifest themselves as highly supersonic (Mach number 20–30) atomic flows, very well collimated over distances ranging from a few AU to several parsecs. They generally consist of a chain of bright and quasi-periodically spaced knots ("the beam") followed by an invisible section, and one or more bow-shaped features aligned with the linear section. Although HH jets were first found about one and a half decade ago (Mundt & Fried 1983), many of their features remain largely unexplained. For example, the excitation of the optical emission in the beam is generally attributed to the presence of shocks that locally heat the gas. These shocks may be formed by hydrodynamical Kelvin-Helmholtz instabilities arising in the interaction with the surrounding medium (see, e.g., Bodo et al. 1994, Stone et al. 1997, Hardee & Stone 1997), or alternatively by velocity variability in the outflow ejection (see, e.g., Stone & Norman 1993, Falle & Raga 1993, 1995). Recent Hubble Space Telescope (HST) observations (Ray et al. 1996, Heathcote et al. 1996, Reipurth et al. 1997) show that all the extended jets observed so far (HH 34, HH 46/47, and HH 111) present morphological characteristics that support the idea of velocity variations in the outflow. In particular, the HST images show that many jet knots can be resolved in bow shocks with the bows pointing away from the source. Such structures can be explained by velocity variations of the flow in the presence of a boundary layer. Furthermore, the capability of the narrow central jet to drive a slower but much more massive molecular outflow, although probable, is not yet firmly established, nor has it been definitely proven that outflows can provide a mechanism to remove excess angular momentum from the disk or star, thereby preventing the accreting star from spinning up to break–up velocity. In order to establish if a reliable dynamical interaction exists between optical and molecular flows, and between mass accretion and ejection, the mass loss and momentum transfer rates of the flows should be known. However, for optical jets large uncertainties affect these estimates, which vary by orders of magnitude, depending on the model assumed.

Send offprint requests to: F. Bacciotti

⋆ *Present address:* School of Cosmic Physics, Dublin Institute for Advanced Studies, 5 Merrion Square, Dublin 2, Ireland (fran@cp.dias.ie)

It becomes clear that a crucial physical parameter for any jet model is the *hydrogen total density* $n_{\rm H}$ of the flow, which is poorly known for HH jets. The total density in a jet cannot be measured directly, contrary to the electron density $n_{\rm e}$, which is easily found from the ratio of the [SII] lines at 6716 Å and 6731 Å (see, e.g. Osterbrock 1989). Hartigan et al. (1994, hereafter HMR94) discussed two principal ways to determine the total density in such objects. The first involves the determination of the luminosity in one forbidden line (Edwards et al. 1987, Cabrit et al. 1990), from which the number of the emitting atoms in the aperture can be deduced. The assumption of a given abundance of the emitting species with respect to hydrogen together with an estimate of the flow radius would then yield the total density in the gas. Spectrophotometric measurements are rare, however, because of the lack of reliable reddening estimates. In addition, the fractional ionization of the emitting species, the excitation temperature and the local filling factor should be known a priori to estimate the average total number density. The second method involves the determination of the hydrogen ionization fraction $x_{\rm e} = n_{\rm H^+}/n_{\rm H} \approx n_{\rm e}/n_{\rm H}$ of the emitting gas. In order to estimate $x_{\rm e}$, HMR94 constructed a grid of planar shock models, and compared the model line ratios with the observed ones. A selected shock model then gives the average ionization fraction in the post shock region, and the total density is derived taking into account that there the gas is more compressed than on average. The results are largely model-dependent: they are greatly affected by the assumed pre-shock conditions and the presence of (unknown) magnetic fields, that may alter the properties of the shocks. Moreover, the assumption of a planar shock geometry is likely a simplification with respect to the actual situation, in which the front may have a curved shape.

Recently, Bacciotti et al. (1995, hereafter called BCO95) developed a spectroscopic diagnostic technique that allows one to find the ionization fraction in the jet beam in a model-independent way. The technique, which used ratios of easy to observe forbidden lines together with Hα, exploited the fact that in the low excitation conditions in the beam of many HH jets the ionization state of oxygen and nitrogen is dominated by *charge exchange* with hydrogen atoms. A first application of the procedure to spectra of HH 34 and HH 111 integrated along the beam provided values of $x_{\rm e}$ of about 0.07 and 0.1, respectively, and an average total hydrogen density of about 10^4 cm^{-3} for both jets.

As demonstrated by HMR94, weak shocks in the beams of HH jets are usually not capable of producing *in situ* an ionization degree larger than a few per cent. On the other hand, BCO95 pointed out that the typical recombination time of the jet gas is of the order of the travel time of the bright jet section, so that if the ionization of the jet is initially produced in the acceleration region (for example by means of a strong steady shock heavily shielded from view) the recombination is sufficiently slow to leave the jet gas considerably ionized even at large distances from the star. If the BCO95 interpretation is correct, the ionization fraction should be observed to gently decrease along the jet axis on spatial scales determined by the product of recombination time and the flow velocity. This prediction is not affected by the presence of weak shocks that may form in the beam, if these contribute to the ionization of the gas at a very low level.

The observational confirmation of such a picture can come from the analysis of spectra spatially resolved along the jet axis. As a first attempt, Bacciotti et al. (1996, hereafter BHN96) examined the optical outflow from RW Aurigae. The results confirmed the suggestion by BCO95: the ionization fraction decreases along the beam according to a well-defined recombination law, from $x_{\rm e} \sim 0.25$ near the star to about 0.02 at a distance of 6 – 7″ ($\sim$ 1000 AU). In RW Aur the total density is again of the order of 10^4 cm^{-3}. It is therefore of great interest to investigate further typical jets in order to obtain a model-independent determination of their fundamental physical parameters, and to establish if the agreement between the "slow recombination" model and the observed trends is confirmed on a larger statistical basis.

Motivated by these ideas we here present the results for a number of outflows: HH 34, HH 46/47, HH 24G, HH 24C/E, HL Tau jet, HH 228 (Th 28). In this way we want to give useful constraints to the models of jet formation and propagation, and possibly to shed light on the dynamical relationships between optical and molecular outflows. In Sect. 2 we describe the observations and the data reduction. Sect. 3 summarizes the physical assumptions underlying the adopted diagnostic technique, and illustrates recent improvements that eliminate possible misinterpretations of the conditions of the emitting gas. In Sect. 4 we describe the results obtained for the "beam" section of the analysed Herbig-Haro jets. A general discussion is presented in Sect. 5, where we summarize our findings and illustrate several interesting physical implications. The main conclusions are given in Sect. 6.

2. Observations and data reduction

The spectra were taken the 20. – 24. February 1987 at the ESO/MPI 2.2-m telescope on La Silla (Chile) using the Boller & Chivens spectrograph. The spectral resolution was about 1.6 Å/pixel and the spatial resolution was 1.76″/pixel. The spectra were reduced following standard procedures, were normalized and wavelength calibrated. In these spectrograms we measured row by row the line intensity integrated over the line width. For a few pixels that were dead or hit by a cosmic ray we interpolated the intensity from the neighbouring unaffected pixels. The background, as well as continuum emission from an extended reflection nebula (e.g., at the base of the HH 46/47 jet), was measured to both sides of the lines and subtracted. We then calculated the line ratios that are necessary for our diagnostic technique (see below) row by row.

3. The diagnostic technique

3.1. Physical foundation and validity

Here, we briefly describe the essential features of the spectroscopic diagnostic procedure and introduce some recent improvements that reduce considerably the errors in the determination of the searched physical quantities. The most commonly

observed lines in Herbig-Haro jets are Hα, the [SII] doublet at 6716,6731 Å, the [OI]$\lambda\lambda$ 6300,6363 and the [NII]$\lambda\lambda$ 6548,6584 lines. The only physical parameter that can be directly determined from the intensity of these lines in a model-independent way is the electron density, from the [SII] doublet (e.g., Osterbrock 1989). Following BCO95 it is possible, however, to determine as well the average ionization fraction $x_{\rm e}$ in the particularly low excitation conditions which apply in the beam section of stellar jets. The procedure is based only on some very general assumptions about the processes that regulate the ionization state of the atomic species involved. The results for the ionization fraction do not depend on any specific mechanism of jet formation and/or evolution.

In jet beams, as in all low-excitation nebulae, sulphur can be considered to be all singly ionized. In its original form, the procedure assumed that the ionization fractions of oxygen and nitrogen were primarily determined by charge exchange reactions with hydrogen. This allowed one to express the population of neutral O and singly ionized N as a function of the hydrogen ionization fraction $x_{\rm e}$. As a consequence, one could determine $x_{\rm e}$ from the comparison of computed and observed line ratios. Charge-exchange as the dominant process controlling the ionization of O and N is suggested by the fact that in the linear section of HH jets there is little observational evidence for high electron temperature or for local or nearby sources of energetic radiation; in addition, previous investigations indicated that a substantial fraction of neutral hydrogen should be present in the beams (see, e.g., Raga 1991, HMR94).

In a second inspection, however, we recognized that although radiative ionization processes are probably not very important in these regions, collisional ionization terms should be implemented in the equations for the ionization state of O and N, given the presence of shocks along the beams. Moreover radiative plus dielectronic recombination can in principle compete with charge exchange. In fact comparing the corresponding reaction rates (see, e.g., Osterbrock 1989) one finds that while for oxygen charge exchange rates are four orders of magnitude larger than the recombination rates (and hence absolutely dominant), for nitrogen the charge exchange rate coefficients are three orders of magnitude smaller than for oxygen, and only slightly larger than the recombination rates. The recombination time scale for nitrogen is, however, about three times smaller than for hydrogen. So, as a first approach it appeared reasonable to assume that after the initial ionization in the jet acceleration region, recombination of N decreases its ionized fraction rapidly to the point where charge exchange becomes dominant, as assumed in the original version of our technique. Quantitatively, comparing the recombination and charge exchange reaction rates at the temperatures of interest, we found that for nitrogen the exclusion of any other mechanism besides charge exchange is a valid approximation only as long as the hydrogen ionization fraction $x_{\rm e}$ is lower than about 0.5.

To overcome these limitations, we recently included in the O and N ionization equations terms describing both collisional ionization, and radiative and dielectronic recombination. Since all the implemented rates depend on the electronic temperature $T_{\rm e}$ only (see below), the ionization state of O and N can also be expressed as a function of $x_{\rm e}$ and $T_{\rm e}$ in this case, and the procedure can be applied as well.

We do not treat photoionization processes. We checked the validity of this approximation in a case in which a stellar source of mildly energetic photons locally maintains a partial degree of ionization in the gas, as a result of the competing effects of photoionization and hydrogen radiative recombination. This physical situation seems appropriate for the outer edges of H II regions, but is unlikely in the beams of stellar jets. Expressing the ionizing flux in terms of the standard ionization parameter Γ, i.e. the ratio between the ionizing photons and the free electrons at a given distance from the source, it is again possible to evaluate the relative importance of photoionization and the other effects as a function of temperature and hydrogen ionization fraction for oxygen and nitrogen. We find here that oxygen is again completely regulated by charge exchange, while for nitrogen the neglect of photoionization is justified as long as $x_{\rm e}$ is lower than 0.5–0.6.

In conclusion, our procedure can be applied to the beams of all those jets in which low excitation and ionization conditions are expected to hold, so that the plasma is mostly neutral. The objects will be selected on the basis of the the absence of lines of high excitation or from highly ionized species as e.g. O^{++}. The method allows, however, to identify regions of both high and low ionization.

3.2. The diagnostic diagrams

The technique uses line ratios from different species, therefore we have to assume a set of relative abundances to compute them. Here, the abundances of nitrogen, oxygen and sulphur relative to hydrogen are taken to be N/H = $1.1\ 10^{-4}$, O/H = $6.0\ 10^{-4}$ and S/H = $1.6\ 10^{-5}$. Now the intensity ratio of any two of the observed lines can be expressed as a function of the electron density $n_{\rm e}$ and the temperature $T_{\rm e}$, which determine the population of the higher levels, and of the hydrogen ionization fraction $x_{\rm e}$, which, together with the temperature, regulates the relative abundances of H^+, N^+ and O^0.

Under the assumption of local ionization equilibrium with respect to the fractional ionization of hydrogen, the following relationship holds for both oxygen and nitrogen:

$$\frac{\rm O^+}{\rm O^0}, \frac{\rm N^+}{\rm N^0} = \frac{(C_{\rm O,N} + \delta_{\rm O,N})x_{\rm e}}{(\alpha_{\rm O,N} - \delta'_{\rm O,N})x_{\rm e} + \delta'_{\rm O,N}} \quad (1)$$

where $C_{\rm O,N}$ are the collisional ionization rates for these species, $\alpha_{\rm O,N}$ are the direct plus dielectronic recombination rates, $\delta_{\rm O,N}$ and $\delta'_{\rm O,N}$ are the direct and inverse charge exchange ionization rates, respectively. Following Raga et al. (1997), we take the collisional ionization and the radiative recombination rates from Landini & Monsignori-Fossi (1990), the dielectronic recombination rates from Landini & Monsignori-Fossi (1990) and Nussbaumer & Storey (1983), and the charge exchange rates from Kingdon & Ferland (1996) and Arnaud & Rothenflug (1985). For each considered ion the emissivity in the lines of interest is found using a code by A. Raga (priv. comm.) that calculates

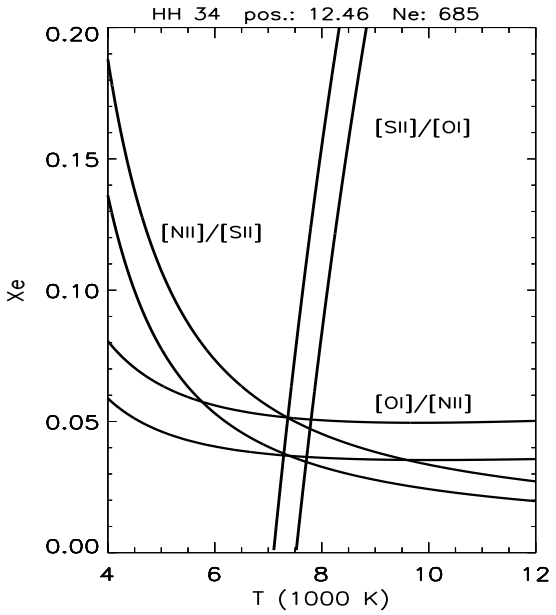

Fig. 1. Example of a diagnostic diagram calculated for the position at 12.″5 in the HH 34 jet. Each strip defines the loci of the $(x_{\rm e}, T_{\rm e})$ values for which the predicted line ratio equals the observed one $\pm$ a 1σ rms error. The intersection of the crossing stripes provides $T_{\rm e} = 7550$ K and $x_{\rm e} = 0.044$ with uncertainties of ± 250 K and ± 0.007, respectively.

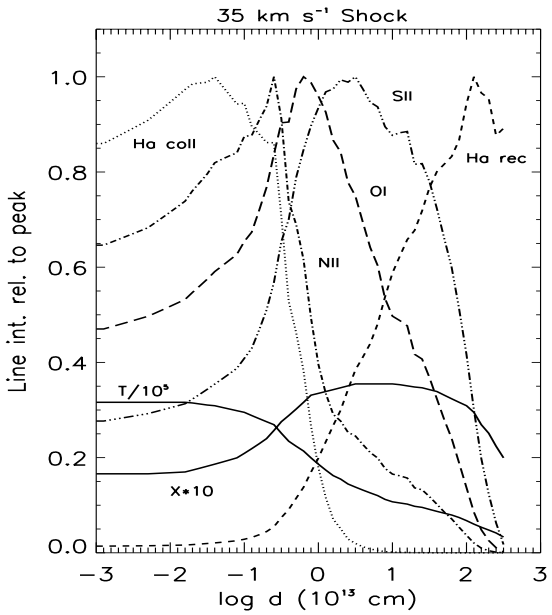

Fig. 2. Post-shock line intensities relative to peak values for the 35 km s^{-1} shock in Fig. 1 of HMR94, with superposed profiles of the temperature and ionization fraction (the former divided by 10^5 and the latter multiplied by a factor 10 for clarity)

the statistical equilibrium populations in the excited levels of the various species as a function of the electron density and the temperature (for details see BCO95, BHN96). Once the electron density is determined from standard methods, any line ratio can be regarded as a known function of $x_{\rm e}, T_{\rm e}$. The ionization fraction is then determined numerically together with the average excitation temperature, comparing calculated and observed line ratios.

In practice, for each position along the jet for which we have measured the relative intensities of the forbidden lines, a diagnostic $(x_{\rm e}, T_{\rm e})$ diagram shows a strip along the loci of the $(x_{\rm e}, T_{\rm e})$ values for which the predicted line ratio equals the observed one including a $\pm 1\sigma$ error. With several different line ratios observed, the intersections of the strips define the values of the local $(x_{\rm e}, T_{\rm e})$ and their uncertainty. An example of such a diagnostic diagram, for one position in the HH 34 jet, is shown in Fig. 1.

Originally, the diagnostic procedure used the [SII]/Hα, [SII]/[OI] and [NII]/Hα ratios, where the simplified notations [NII], [OI] and [SII] stand for the sum of the two [NII] lines at 6548 and 6584 Å, the sum of the two [OI] lines at 6300 and 6363 Å, and the sum of the sulphur lines at 6716 and 6731 Å, respectively. As recently demonstrated by Pat Hartigan (priv. comm.), the Hα line, however, cannot be used for a determination of the physical parameters of the emitting gas in this procedure. This is due to the fact that Hα emission can be produced both by collisional excitation, arising at high temperatures (several 10^4 K) and moderate ionization, and by recombination, mainly occurring at low temperatures (less than 6–7000 K). In the cooling region behind a shock front steep temperature gradients are present, and both emission mechanisms contribute to the observed Hα line. This is evident in Figs. 2 and 3, that show the post-shock peak-normalized intensity for each line of interest (collisional Hα, recombination Hα, [SII] 6716+6731, [OI] 6300+6363, [NII] 6583+6548) for a 35 km s^{-1} and a 70 km s^{-1} shock. We calculated the intensity profiles with our radiative code, extracting $x_{\rm e}$, $T_{\rm e}$ and the compression factor from the plots in Fig. 1 of HMR94.

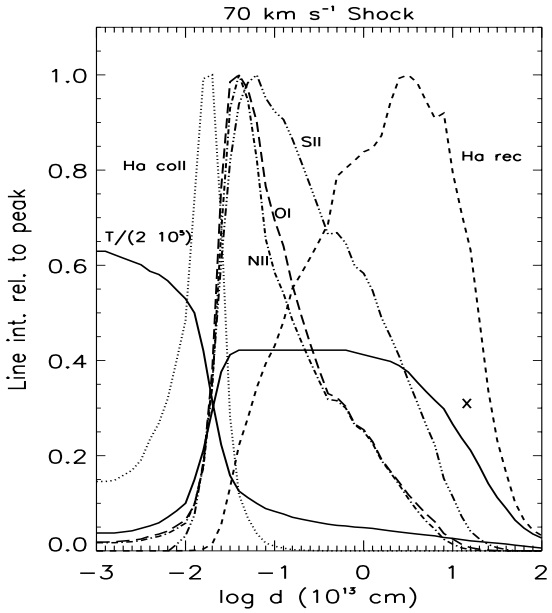

Fig. 3. Post-shock line intensities relative to peak values, temperature (divided by a factor 2 10^5) and ionization fraction for the 70 km s^{-1} shock in Fig. 1 of HMR94

The line emission arises on a scale of 10^{13} – 10^{15} cm, which at the typical distance of HH jets (at least 100 pc) is not spatially resolved in ground-based observations. Thus, it is not possible to separate the two Hα contributions, and the use of the Hα line in the diagnostic may lead to misinterpretations of the physical conditions of the emitting gas. The forbidden lines, on the contrary, come from regions characterized by intermediate temperatures and ionization fraction, which are rather similar one to each other. Therefore, the Hα line is not used in our diagnostic procedure, and the diagrams are constructed from the ratios [SII]/[OI] (sensitive to both $x_{\rm e}$ and $T_{\rm e}$), [OI]/[NII] (sensitive mainly to $x_{\rm e}$) and [NII]/[SII] (to check consistency).

3.3. Validation of the technique

We compared the results of this procedure to the predictions of the radiative shock models in HMR94. First, we tested if similar average values for $x_{\rm e}$ and $T_{\rm e}$ will be obtained for the regions in which the different species radiate. For doing this, we determined the average values of $x_{\rm e}$ and $T_{\rm e}$ weighted by the flux of the various lines from Figs. 2 and 3 as:

$$< x_{\rm e} >, < T_{\rm e} >= \int x_{\rm e}(z), T_{\rm e}(z) \cdot F(z) dz / \int F(z) dz$$

where $F(z)$ is the flux in the different lines and z is the (linear) distance from the shock front. The resulting average properties for the emission regions of the various ions are listed in Table 1. They show that for both shock speeds, the average $x_{\rm e}$ values are remarkably similar for the forbidden-line emitting species, and close to the value of the $x_{\rm e}$ plateau of Figs. 2 and 3. Therefore, they can be considered representative of the conditions of the emitting gas. The temperature, however, varies more over distance, though the average values are similar for the various forbidden lines. The "average temperature" can therefore only be considered as a rough indication of the excitation temperature of the various ions.

In a second step, we checked if at a given "finite" spatial resolution similar results will be obtained through our diagnostic procedure. This time, we integrated the line emission given in Figs. 2 and 3, because these region would not be resolved in our spectra. For the integrated line intensities we constructed then our diagnostic diagrams (Figs. 4 and 5), using the line ratios [SII]/[OI], [OI]/[NII] (and [NII]/[SII] to check consistency). We take as $< n_{\rm e} >$ the post-shock electron density weighted by the [SII] lines (as it would be if one would derive it from the observations): this turns out to be 212 cm^{-3} for the 35 km s^{-1} shock and 4700 cm^{-3} for the 70 km s^{-1} shock. The diagnostic then provides $x_{\rm e} = 0.033$ and $T_{\rm e} = 8100$ K for the 35 km s^{-1} shock, while for the 70 km s^{-1} shock we derive $x_{\rm e} = 0.347$ and $T_{\rm e} = 7600$ K. Indeed, the derived values agree very well with the values quoted in Table 1, i.e. our method reproduces the ionization fractions and the excitation temperature of a shock code averaged over the forbidden-line emission region well. In particular, the resulting values are close to the [SII]-weighted averages. This is desirable, since also the electron density is measured from the [SII] lines.

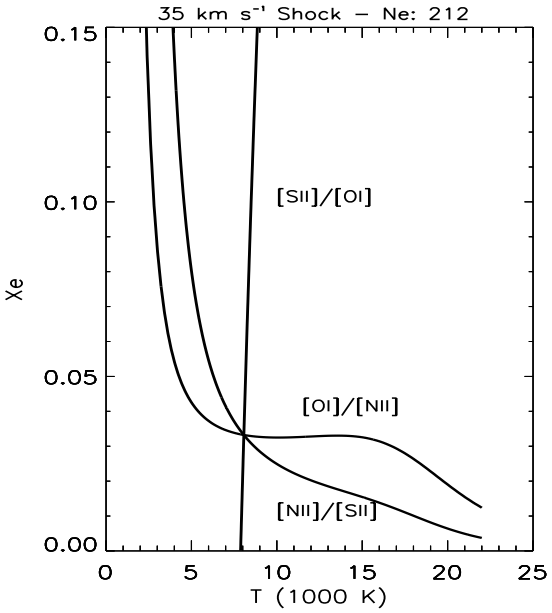

Fig. 4. Diagnostic diagram obtained for the integrated line ratios of the 35 km s^{-1} shock in HMR94. The curves cross at $x_{\rm e} = 0.033$ and $T_{\rm e} = 8100$. The values are error-free here, since the input line ratios are calculated numerically.

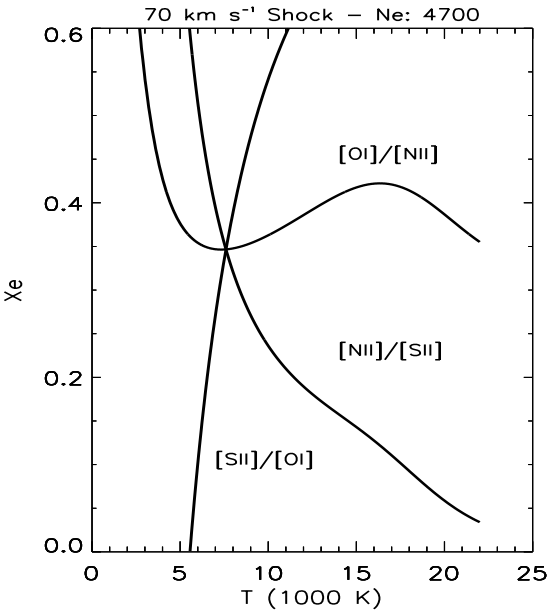

Fig. 5. Diagnostic diagram for the integrated line ratios of the 70 km s^{-1} shock in HMR94. One obtains here $x_{\rm e} = 0.347$ and $T_{\rm e} = 7600$.

Table 1. Flux-weighted average $x_{\rm e}$ and $T_{\rm e}$ in the shock cooling region.

	35 km s^{-1}		70 km s^{-1}	
line	$< x_{\rm e} >$	$< T_{\rm e} >$	$< x_{\rm e} >$	$< T_{\rm e} >$
[SII]	0.032	8070	0.336	7650
[OI]	0.033	9090	0.364	9180
[NII]	0.033	9950	0.378	9640
Hα rec	0.027	5830	0.219	4810
Hα coll	0.028	22710	0.281	64390

We also tested if our technique gives results similar to those of HMR94 when applied to observed data. In that paper the authors examine three prototypical jets, and find the average ionization fractions comparing observed spectra integrated over the brightest part of the beams with their grid of shock models. From the observed [NII]/[OI] ratios HMR94 find for HH 34, HH 46/47 and HH 111 $< x_{\rm e} >= 0.026, 0.055$ and 0.052 respectively. With the same observed parameters, our diagnostic provides $x_{\rm e} = 0.027$, 0.070 and 0.064. These results are consistent within about 20% with the ones given in HMR94. The difference could come from different elemental abundances, the peculiar preshock density or ambient magnetic field adopted in the shock models. Therefore, we conclude that the new version of our method gives results in agreement with the HMR94 shock calculations (see also Sect. 5.1). While the improved technique in most cases provides ionization fractions similar to those found with the original version, major differences are found for the average $T_{\rm e}$, which can be substantially higher than the 5000–6000 K that were usually derived. Higher values of the excitation temperature are, however, much more reasonable in the context of shock excitation. It must be remembered that both the ionization fraction and the temperature we derive are averages weighted by the flux of the considered forbidden lines. On the other hand, the shock models show that the gas ionization fraction maintains an almost constant value along a large portion of the cooling region, while temperature varies rapidly by two orders of magnitude with distance from the shock front. As a consequence, the ionization fraction we find can be considered highly representative of the emitting gas as a whole, whereas the provided "$T_{\rm e}$" is only a rough indication of the local excitation temperature.

One could ask if our diagnostic procedure is also applicable if the gas entering the shock has a substantial pre-ionization. Then, a certain amount of O and N could be ionized through charge exchange and collisional ionization just behind the front. Since the excitation of the forbidden lines grows rapidly with temperature, this might produce two separate regions of emission: one close to the shock front at high temperature and moderate ionization and the other in the intermediate layers with lower $T_{\rm e}$ and higher ionization. As with Hα, we would have the problem of not being able to distinguish the two regions at our resolution. A proper answer to this question would require the determination of the ionization structure of O and N running a shock model into a partially ionized medium. As a zero-order approach, however, one can add a predetermined value to the shock ionization fraction profile in HMR94, and evaluate the line emission profiles as a function of the distance from the front (as in Figs. 2 and 3). We examined the cases of the 35 km s^{-1} shock with additional ionizations of $x_1 = 0.2$ and 0.4, and of the 70 km s^{-1} shock with an additional ionization $x_1 = 0.2$. As expected, close to shock front the emission in the forbidden lines is enhanced with respect to the case of propagation into a neutral medium; the peak emission, however, is again localized in the intermediate region, thanks to the increase of the ionization in that zone and, more important, to the compression of the post-shock gas. Therefore, a determination of the $x_{\rm e}$ plateau value is still possible: the $< x_{\rm e} >$ and $< T_{\rm e} >$ averages weighted by the emission of the forbidden lines are similar to each other, and close to the values determined by the diagnostics within better than 10–15%.

The amount of dust extinction towards the various positions along the jets is generally unknown, and may even vary along the beam of a single object. Therefore, we did not apply any dereddening correction to the relative intensity of the lines in our analysis. On the other hand, reddening is not expected to have a big affect on our diagnostic results, due to the proximity in wavelength of the lines used. We estimated the influence of reddening assuming a fiducial value for the visual extinction of $A_{\rm V} = 3$ mag (such an extinction has been estimated towards a few T Tauri stars, including T Tau itself). Using this value and the standard interstellar extinction curve of Savage & Mathis (1979), one finds that the [SII]/[OI] ratio calculated from the observed values would be overestimated by about 18% with respect to the emitted ratio, while both the [OI]/[NII] and the [NII]/[SII] ratio would be underestimated, by about 9%. As a consequence, in a 'dereddened' diagnostic diagram the [OI]/[NII] contours would be slightly shifted towards lower ionization, while the [SII]/[OI] and the [NII]/[SII] contours would be shifted toward higher temperatures. Recalculation of the jet parameters in several selected positions in various jets assuming such a reddening has confirmed that due to the limited wavelength range of the used lines and to our choice of the line ratios, the uncertainty in the determination of $x_{\rm e}$ and $T_{\rm e}$ because of uncorrected reddening is in any case not larger than the measurement error, being at most about 8–10% for the ionization fraction, and about 15% for the temperature.

4. Results

In this section we present the results of the application of the diagnostic technique to the beam section of six Herbig-Haro jets: HH 34, HH 46/47, HH 24G, HH 24C/E, the HL Tau jet and HH 228 (Th 28 jet). Each case is described in detail in the following, while a general discussion, together with two tables summarizing the main results is presented in the next section.

4.1. HH 34

One of the most spectacular examples of a Herbig-Haro jet is the HH 34 outflow, which lies in the L1641 complex, at a distance of $\sim$ 480 pc (Reipurth et al. 1986, Bührke et al. 1988). South of the source HH 34 IRS lies the blueshifted HH 34 jet, a 25″ long chain of well-aligned bright knots, which is followed by a section where very little emission is seen, and by the large bow shaped feature HH 34S at a distance of 95″ from the source. In the following, we limit ourselves to the study of the beam of the jet, from a few arcseconds to about 27″ from the source. In the beam, which is inclined at roughly 24° to the plane of the sky, the emitting gas parcels move with a space velocity of $\sim$ 220 km s^{-1} (Eislöffel & Mundt 1992, Heathcote & Reipurth 1992). The average radius of the knots is $\sim 0\farcs4$ ($\sim 2.9\,10^{15}$ cm

at the assumed distance of 480 pc) as derived both from ground based and HST observations (Raga et al. 1991, Ray et al. 1996).

Our results for the HH 34 jet are presented in a column of graphs in Fig. 6. Panel *a* shows a contour plot of a [SII] image of the object. Intensity tracings along the beam integrated over the line widths of Hα, [SII] 6716+6731, [NII] 6548+6584, and of the sum of the two [OI] lines at 6300 and 6363 Å, all normalized to the Hα peak, are shown in panel *b*. They provide an overview of the line brightness and the excitation conditions with distance from the source.

In panel *c* we plot the electron density as derived from the [SII] line ratio; in the bright part of the beam it is observed to increase progressively to knot J (following the nomenclature by Raga et al. 1991), the second brightest knot in the flow. Beyond knot J the jet apparently flares out and $n_{\rm e}$ falls again. Contrary to the electron density, the ionization fraction (panel *d*) is found to decrease from $x_{\rm e} = 0.145$ at the beginning of the flow to very low values ($x_{\rm e} \sim 0.02$) in the bright portion of the jet. Among the jets of our sample, the HH 34 flow apparently is the most neutral on average: $x_{\rm e}$ is lower than 0.05 in the brightest section. At position $z = 5\farcs3$, coincident with the location between knots B and C, the ionization fraction jumps up to about 0.25 and simultaneously a local enhancement in the electron density is observed. At our spatial resolution we cannot decide if indeed in this region the flow gets reionized, or if this behavior is mimicked by a high measurement error due to the faintness of this part of the jet. Apart from this point, the ionization nicely follows a recombination curve calculated assuming that on average the gas parcels flow in a set of nested cones, whose shape is specified by the initial jet radius and a constant opening angle. Other required input parameters are the average jet speed, the jet distance, an estimate of the inclination angle of the beam with respect to the plane of the sky, and an estimate of the initial electron density. See the Appendix for a description of this model. Our best-fit curve for the HH 34 jet turns out to have a negative opening angle $\theta = -1\fdg6$, i.e., the jet is slightly converging. This is in accordance with the behavior of $n_{\rm e}$, and with previous investigations by Raga et al. (1991), who measured the jet diameter directly on optical images. Ray et al. (1996), however, find a much more complex structure on high resolution images from HST: at least knots I and J clearly show a bow shape, and an almost perfect anticorrelation between peak intensity and jet width is observed all along the flow.

The average excitation temperature of the forbidden lines emission region also is found to mildly decrease from about 10^4 K at the beginning of the flow to about 6000 K at the end of the bright section (see panel *e*). Then it rises again to ~ 6500 K in the last two positions, where the faint bow-shaped knot L is located. A small enhancement in the ionization fraction is simultaneously observed. The results for these last two positions may, however, be affected by the faintness of the lines.

Panel *f* then presents the total hydrogen density as resulting from $n_{\rm H} = n_{\rm e}/x_{\rm e}$. Since our results are not derived from a shock calculation, we cannot identify a compression factor to be applied to the resulting hydrogen density, as in HMR94. Here we use as total density the ratio between the electron density and

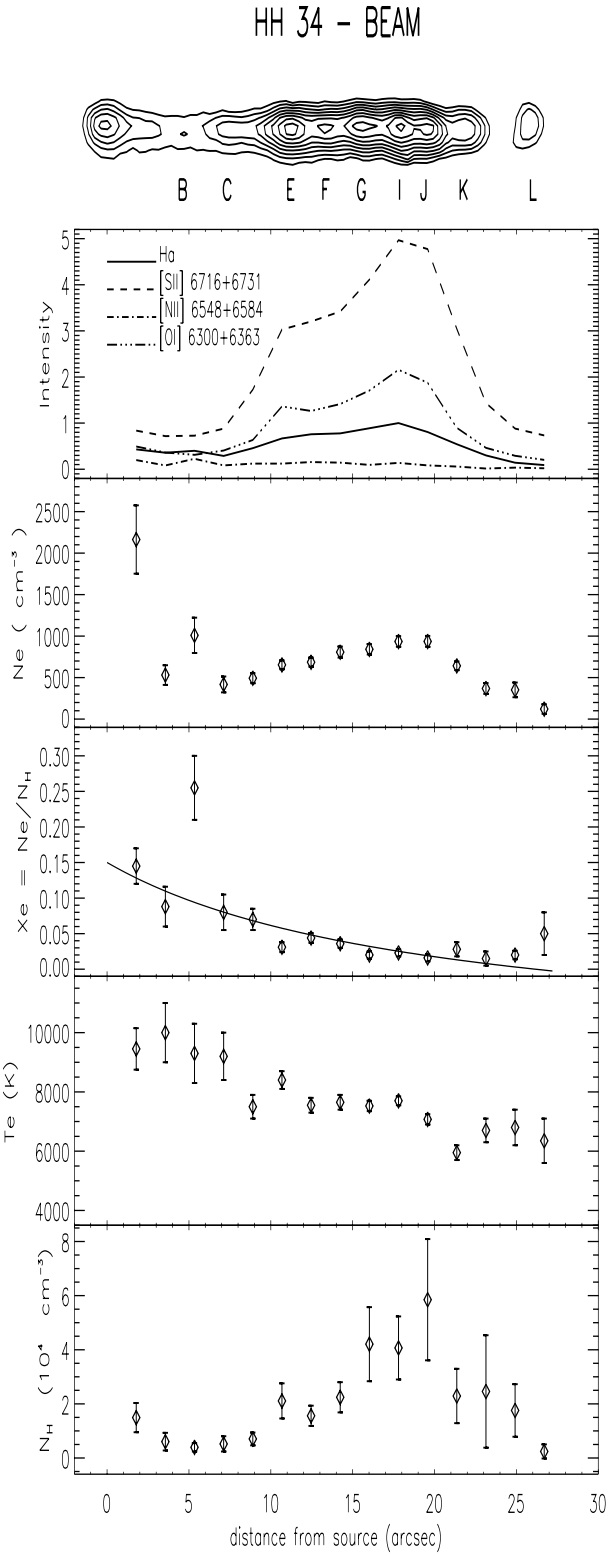

Fig. 6a–f. Physical conditions along the beam of the HH 34 jet. From *top* to *bottom*: **a** contour plot of a [SII] image of the jet, **b** intensity tracings in the various lines normalized to the Hα peak (see text), **c** electron density derived from the [SII] lines ratio, **d** hydrogen ionization fraction $x_{\rm e}$ and superimposed recombination curve (see text), **e** average excitation temperature of the forbidden line emission region, **f** total hydrogen density $n_{\rm H} = n_{\rm e}/x_{\rm e}$

ionization fraction (see below). The total density profile along the jet shows a similar behavior as the electron density: after a slight decline prior to $z = 5''$ the total density increases from about 4000 cm^{-3} to 5.8 10^4 cm^{-3} near knot J. Then it decreases again to values close to the initial values. No jump in the total density profile is evident at position 5.″3, where an abrupt change in the electron density is seen.

From the total density a mean value of $n_{\rm H} \sim 2.0\ 10^4$ cm^{-3} along the jet can be deduced. With a mean molecular weight of 1.24 the average mass loss and momentum rates for the HH 34 jet then are $\dot{M} = \pi r_{\rm j}^2 \rho v_{\rm j} \approx 3.7\ 10^{-7}$ M$_\odot$ yr^{-1} and $\dot{P} = \dot{M} v_{\rm j} = \pi r_{\rm j}^2 \rho v_{\rm j}^2 \approx 8.1\ 10^{-5}$ M$_\odot$ yr^{-1} km s^{-1}. These values are very close to the values found in BCO95 from a spectrum integrated all along the beam, and a factor 2 larger than those of HMR94, who derive an average ionization half of ours, but then apply a correction factor 0.25 for postshock compression (see below).

4.2. HH 46/47

The HH 46/47 outflow lies at the edge of the Gum nebula at a distance of roughly 450 pc. The jet consists of a long wiggling chain of knots, more pronounced in the first half of the flow and fainter in the second half (see, e.g. Eislöffel & Mundt 1994). The knots at the base of the jet are bright in [SII] and Hα and are spatially resolved with an apparent radius of about 0.″4 corresponding to about $2.7\ 10^{15}$ cm. On HST images the numerous features of the fainter section appear as narrow wisps and filaments (Heathcote et al. 1996); probably they represent shocks resulting from the interaction of the jet with the surrounding medium. The visible jet terminates in an extended bow shock, HH 47A. On HST images HH 47A clearly appears as a clumpy region prominent in [SII] 'sandwiched' between the forward bow shock and the Mach disk, both luminous in collisionally excited Hα. Recent kinematical studies found an inclination angle of about 28° of the flow to the plane of the sky and an average velocity of about 300 km s^{-1} (Eislöffel & Mundt 1994, Morse et al. 1994).

Here, we analyse the north-western part of the flow from its base to HH 47A (Fig. 7, panel *a*). The excitation conditions vary considerably along the flow (panel *b*). The bright reflection nebula at the base of the jet severely hampers the determination of the physical quantities in this region. Although the reflected light was carefully subtracted larger errors in the resulting values for positions $z < 15''$ indicate residual contamination. The electron density (panel *c*) steadily decreases from ~ 1200 cm^{-3} close to the source to about 100 cm^{-3} at $z = 45''$. In the following faint section $n_{\rm e}$ is very low ($\sim$ 10–30 cm^{-3}), while it increases again in the working surface, where it reaches its local maximum value (~ 350 cm^{-3}) just before the location where the forward shock should be found.

The ionization fraction $x_{\rm e}$ also decreases on average along the first section of the flow (panel *d*). From the source to 10″ it falls from 0.23 to 0.050, then it rises again to 0.145 at position $z = 16''$, and then floats around 0.12 until $z = 30''$. Further out, the ionization degree falls substantially to $x_{\rm e}$ = 0.02 at the end of the first bright segment of the jet. After $z = 45''$, but

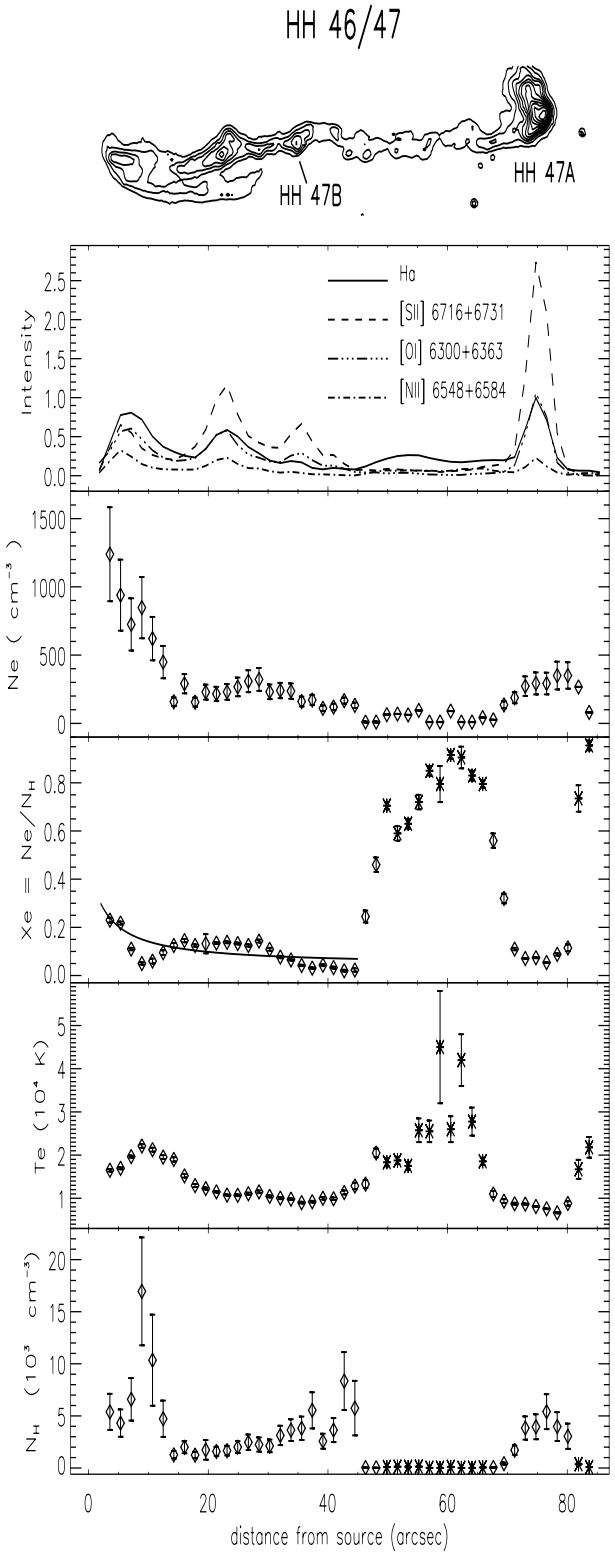

Fig. 7a–f. Physical conditions along the beam of the HH 46/47 jet. Panel description as in Fig. 6. The values denoted by an asterisk are results for a region where the applicability of our technique becomes critical.

before HH 47A, the technique qualitatively indicates that the jet is highly ionized, the resulting $x_{\rm e}$ varying between 0.5 and 0.9. This result has to be taken with caution though, because here the extremely low gas density and the high ionization make one to suspect that photoionization effects produced by the shock fronts themselves may not be negligible. In the HH 47A the ionization fraction decreases to about 0.055 and then jumps up again close to the forward shock of the working surface. The recombination curve superimposed along the first 45″ of the jet would correspond to an opening angle of $\theta = 1\overset{\circ}{.}0$, i.e. a slightly diverging jet.

The average temperature (panel *e*) varies between $2.2\ 10^4$ and $9.0\ 10^3$ K along the bright part of the beam. Values as high as $4.5\ 10^4$ K are reached in the following faint section, but no strong increase is seen at the location of the Mach disk and the forward shock of HH 47A.

In panel *f* we show the derived total density $n_{\rm H}$. In the bright part of the flow $n_{\rm H}$ varies in the range 1.2–17.0 10^3 cm^{-3}. Similar to the electron density, $n_{\rm H}$ is higher near the first bright knot and in the working surface, while it is very low in the faint section. It increases consistently also at the end of the bright section, due to the extremely low ionization. Taking a mean $n_{\rm H} = 4.3\ 10^3$ cm^{-3} over the first 45″, a jet speed of 300 km s^{-1} and a radius of 2.7 10^{15} cm, we derive mean mass loss and momentum transfer rates of $\dot{M} = 9.4\ 10^{-8}$ M$_\odot$ yr^{-1} and $\dot{P} = 2.8\ 10^{-5}$ M$_\odot$ yr^{-1} km s^{-1}. These values are about one quarter of those found by HMR94. From their planar shock models these authors found an average ionization fraction of 0.036 (see the discussion in the next section). They adopt as average electron density $n_{\rm e} = 250$ cm^{-3}, and then correct their total density estimate for a compression factor 0.2 leading to $n_{\rm H} = 1400$ cm^{-3}, less than one third of ours. They assumed, however, a mean jet radius of 1.″3 arcseconds while we used 0.″4 (from HST images).

4.3. HH 24C/E

The HH 24 complex lies in the NGC 2068 nebula at a distance of 480 pc. At least three separate outflows are emanating from this complex (see, e.g. Mundt et al. 1991, hereafter MRR91, Eislöffel & Mundt, 1997). The HH 24C/E jet, described by Solf (1987), spans over 100″ in the sky, and is apparently accelerated by the invisible source SSV 63 (Strom et al. 1976). The HH 24C jet consists of a straight blueshifted chain of knots north-west from the source at a distance of 14″ to 30″. The counterjet, HH 24E, extends from −2″ to −17″ from the source (see also Eislöffel & Mundt 1997). At −23″ from the source one finds the bright condensation HH 24A, that may, however, be part of a separate outflow, the HH 24MMS jet. Measured radial velocities are −180 km s^{-1} in the C jet and about 150 km s^{-1} in the E counterjet (MRR91). Both structures have roughly constant spatial widths in their brightest sections, on average about 1.″1 for HH 24C and 0.″7 for HH 24E, which correspond to 8 10^{15} and 5 10^{15} cm, respectively, at the assumed distance of 480 pc (MRR91).

HH 24C presents conditions of mild excitation (Fig. 8, panel *b*). Correspondingly the ionization fraction never falls below 15% in the bright region (panel *d*). The ionization data points do not follow a monotonic trend. Instead, $x_{\rm e}$ is oscillating around a mean value of ∼ 0.25, with a slight increase in the fainter middle section of the flow, where the gas is apparently reionized: contrary to HH 34 the ionization data points are better fit by two different recombination curves. For this jet no determination of the inclination angle is available, therefore we calculated for each jet section three sets of recombination curves, corresponding to inclination angles to the plane of the sky of 10°, 25°, and 40°. In any of these cases the best-fit recombination curves for the first jet section correspond to a flow slightly converging by an angle of −2°, while the second beam section is better described assuming an opening angle of 1°. As the best-fitting inclination angle we find 20° – 30°. The electron density (panel *c*) decreases on average along the flow, but peaks at the positions of the two brightest knots. At knot C2 (following the denomination of MRR91), at $z = 19.''5$, we find 880 cm^{-3}, and at knot C5, at $z = 28.''5$, we find 470 cm^{-3}. The average excitation temperature starts at $2.0\ 10^4$ K at the beginning of the flow (panel *e*), then falls by 10^4 K and increases again to reach $2\ 10^4$ K at position $z = 32.''3$, i.e. at the end of the bright beam section. Apart from position $z = 32.''3$, the behavior of the total density (panel *f*) is similar to that of $n_{\rm e}$: they both follow the intensity profile of the lines. The average total density is about $2.1\ 10^3$ cm^{-3}. The fact that both the electron density and the total density are rather low helps to understand how a moderate ionization degree can be maintained over large distances, contrary to, e.g., the HH 34 jet. Under such low density conditions recombination is disfavoured and therefore the ionization degree can be maintained over a relatively long distance. Assuming that the average density is constant on the transverse jet section, and taking a jet velocity of 425 km s^{-1} and a jet radius of $0.''55$, the average mass loss rate obtained for this jet is $\dot{M} = 1.4\ 10^{-7}$ M$_\odot$ yr^{-1}, while the momentum transfer rate is $\dot{P} = 6.0\ 10^{-5}$ M$_\odot$ yr^{-1} km s^{-1}.

In HH 24E, moderately low excitation conditions are present along the jet. In HH 24E the ionization degree (Fig. 9, panel *d*) shows two pronounced jumps at positions $z = -10.''7$, i.e. just after knot E, and $z = -21.''3$, i.e. at the beginning of the bright condensation HH 24A. The ionization fraction decreases smoothly within each of the three sections, albeit along three different recombination curves. On average, it becomes progressively higher from one section to the next: $x_{\rm e}$ varies from ∼ 0.15 to ∼ 0.06 in the first section, from ∼ 0.36 to 0.17 in the second, and from 0.38 to ∼ 0.3 in the third section. As in HH 24C, the jet inclination angle is unknown, so that for each different jet section we calculated three sets of tentative curves corresponding to 10°, 25°, and 40°. The best fit in each jet section is obtained for opening angles of 2°, 0°, and 1°, respectively. Interestingly enough, the data points in HH 24A are best reproduced assuming an inclination angle of only 10°, which is quite lower than the 20° – 30° inclination angle that describes the first two sections of HH 24E and HH 24C. This could be evidence that HH 24A may indeed belong to the nearby HH 24MMS jet,

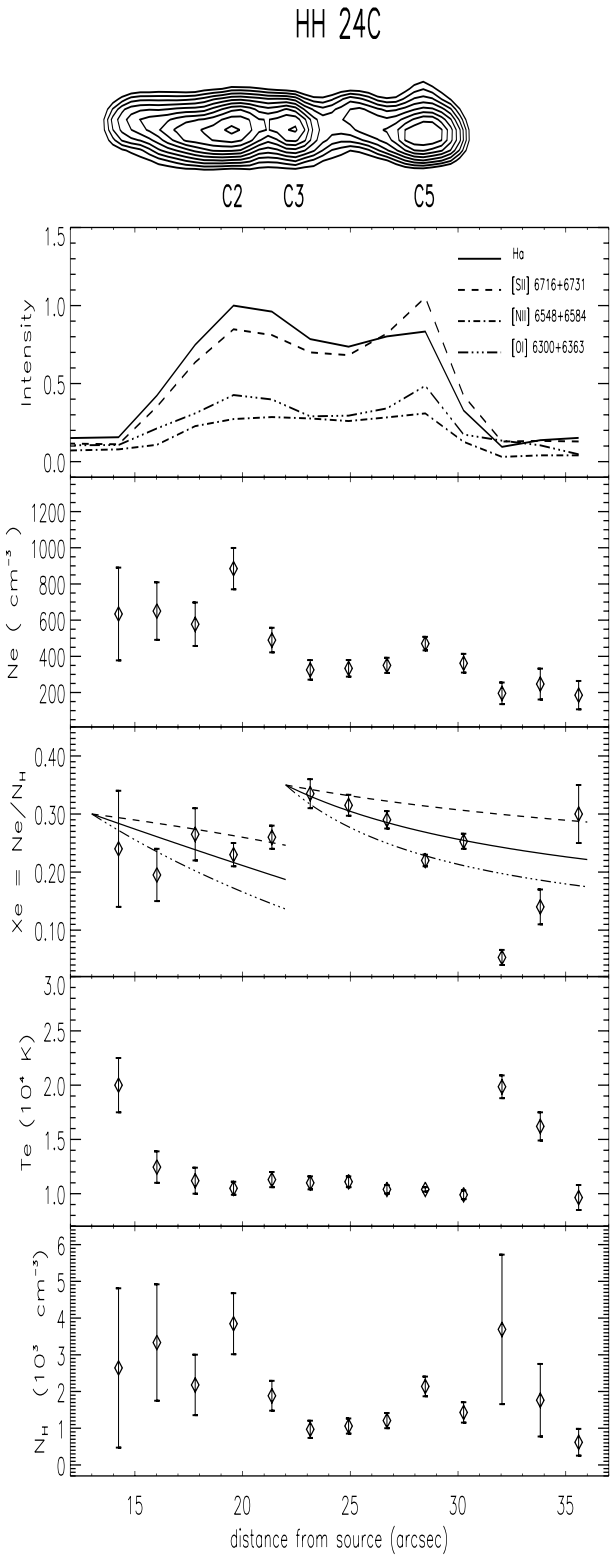

Fig. 8a–f. Physical conditions along the beam of the HH 24C jet. Panel description as in Fig. 6. The superimposed recombination curves are calculated for a jet inclination angle of 10° (dashed lines), 25° (solid lines) and 40° (dash-dotted lines). The source is located to the left.

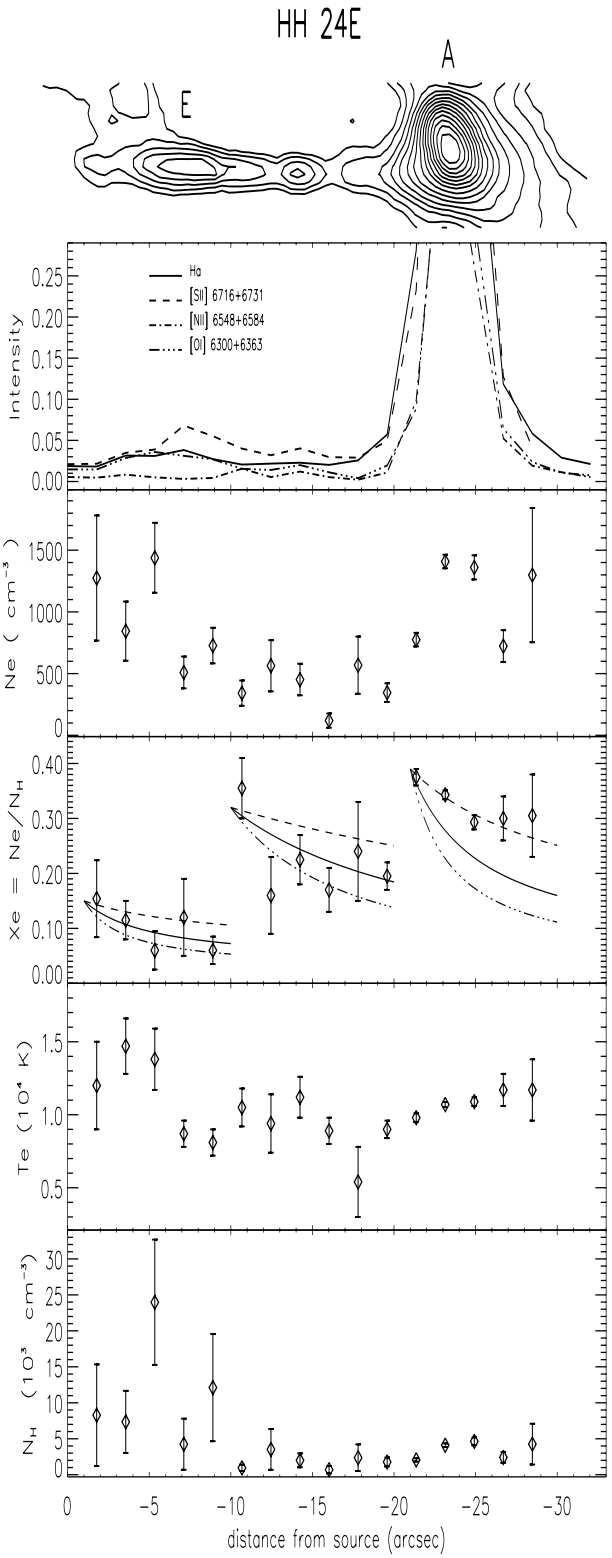

Fig. 9a–f. Physical conditions along the beam of the HH 24E counter jet. Panel description as in Figs. 6 and 8. Note marked enhancements in the ionization fraction at positions $z = -10\farcs6$ and $z = -21\farcs3$ and the subsequent decline in the direction away from the source (see text).

and not to the HH 24E jet. The average excitation temperature (panel *e*) decreases from 1.5 10^4 K to 1.0–1.1 10^4 K near knot A. An isolated marked decay at 5400 K is observed at position $z = -17''.8$, where, however, the jet is very faint. In knot A the electron density increases from ~ 350 to ~ 1400 cm^{-3}, while no apparent enhancement is seen near the first jump at $z = -10''.7$. On the other hand, the derived total density (panel *f*) is higher in the first section of the flow than in knot A (if allowance is made for the large errors in the first positions). As a mean along the flow one can take $n_{\rm H} = 5.6\ 10^3$ cm^{-3}, which, together with an assumed 25° inclination angle, 2.5 10^{15} cm radius and 150 km s^{-1} radial velocity of the jet, yields a total mass loss rate of $\dot{M} \approx 1.3\ 10^{-7}$ M$_\odot$ yr^{-1} and a total momentum supply rate $\dot{P} \approx 4.5\ 10^{-5}$ M$_\odot$ yr^{-1} km s^{-1}.

4.4. HH 24G

The HH 24G outflow is apparently emanating from the IR source SSV63 NE, which lies $\sim 30''$ to the south-west of this jet (MRR91). It consists of two separate condensations which are rather diffuse in appearance, followed by a small clump at the end of the flow. The jet is blueshifted and has a radial velocity of -130 km s^{-1}. Its average width in the brightest region is $\sim 5''$ corresponding approximately to a diameter of 3.6 10^{16} cm.

According to its [SII]/Hα ratio (Fig. 10, panel *b*) the HH 24G jet appears to be of low excitation. The average ionization (panel *d*), however, turns out to be higher in the second portion of the flow. As in HH 24E, re-ionization episodes appear to be present along the beam, the first one being at $z = 53''.4$, in the faint bridge between the diffuse knots, while a second one at $z = 64''$ is related to the intensity maximum in HH 24G2 (nomenclature as in MRR91). At the same position also the electron density peaks (~ 600 cm^{-3}), while the temperature reaches its maximum value in the faint bridge ($\sim 1.14\ 10^4$ K at position $z = 48''.1$). Another jump might occur at $z = 46''.2$, but our measurement accuracy is not sufficient to ascertain its presence. Therefore, we tentatively superimposed three sets of recombination curves to the $x_{\rm e}$ data points, calculated assuming inclination angles of 10°, 25°, and 40°, as for HH 24C/E. The results are better reproduced assuming an inclination angle to the plane of the sky of about 30° in this jet. The best-fit opening angles are, however, larger than in the previous cases: in the first section the jet apparently opens up at $\theta_1 = 2°$, after the bridge it seems to reconverge following cones with an angle of $\theta_2 = -10°$ and it finally opens up again with $\theta_3 = 20°$. As in HH 24E, the smooth recombination decreases are observed on the far side of the jump with respect to the source (i.e. downstream), and each subsequent event puts the jet gas to a slightly higher degree of ionization. Notably, the second recombination section is associated with an increase in both the electron and total density from the bridge to the end of the flow.

Finally, we note that as in HH 24C/E a moderately high degree of ionization is associated with low $n_{\rm e}$ and $n_{\rm H}$. The electron density is 200–300 cm^{-3} for a large portion of the flow while the total density scatters around 1400 cm^{-3}: apparently the jet is lighter in the first section and denser in the second.

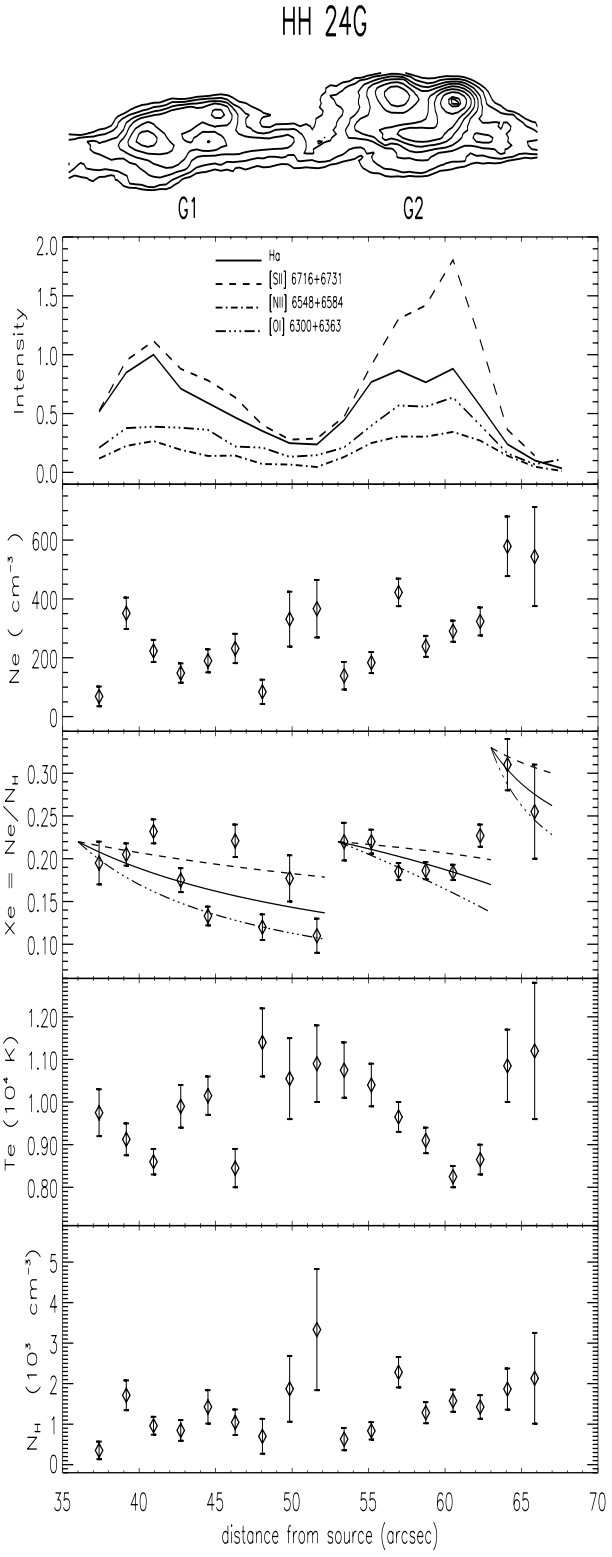

Fig. 10a–f. Physical conditions along the beam of the HH 24G jet. Panel description as in Fig. 6. The superimposed recombination curves are calculated for a jet inclination angle of 10° (dashed line), 25° (solid line) and 40° (dash-dotted line). The source is on the left.

Because of its rather large average radius, the mass loss and momentum transfer rates in HH 24G are not smaller than those of the other jets. Assuming a constant density in the jet section and an inclination angle of 30° yields $\dot{M} = 1.2\ 10^{-6}\,\mathrm{M}_\odot\,\mathrm{yr}^{-1}$ and $\dot{P} = 3.1\ 10^{-4}\,\mathrm{M}_\odot\,\mathrm{yr}^{-1}\,\mathrm{km\,s}^{-1}$. These large values could, however, easily be reduced by an order of magnitude, since this flow appears to be rather clumpy (MRR91) so that the effective jet radius may be much smaller than the 2.″5 we used.

4.5. HL Tau jet

North-east of HL Tau, there is a long jet of at least 50″ with a fainter counterjet on the opposite side of HL Tau, only seen in [SII] images. HL Tau is surrounded by a diffuse nebulosity which is bright in Hα, and which did not allow us a reliable application of the technique in the proximity of the source. We studied, however, the physical properties of the bright, $\sim 20''$ long structure north-east of HL Tau beyond 15″ from the star to the condensation at $z = 45''$ from HL Tau (knot HL-E in Mundt et al. 1990).

The HL Tau jet is blue-shifted with a velocity of about $-180\,\mathrm{km\,s}^{-1}$. The width measured from Hα images ranges from 1″ to 3″ and is larger than the corresponding width in [SII] by more than 50% (Mundt et al. 1990). On the basis of the broad Hα and narrow [SII] line profile, the authors interpreted the larger jet width in Hα in terms of turbulent entrainment of ambient gas at the boundary of the flow. Possible terminal working surfaces have been found recently by Lopéz et al. (1995).

The jet seems to be rather diffuse: in accordance with the estimate by Mundt et al. (1990) the electron density is low everywhere, varying around 300 cm^{-3} on average (see Fig. 11, panel *c*). N_e stays almost constant along the beam of the HL Tau jet, while it decreases in the HL-E knot. Apart from the first position, that could be affected by the faintness of the [SII] lines, in the bright section of the flow x_e steadily increases from about 0.14 to about 0.36 (panel *d*). This behaviour is opposite to that of the other jets examined so far. The ionization, however, can be produced in the turbulent boundary layer whose presence has been suggested on the basis of the Hα line profile, instead of by a violent event at the base of the jet (Mundt et al. 1990). If this is the case, the ionization fraction could be 'pumped' all along the length of the flow. As a consequence, no recombination curve can be drawn for this jet. After position z= 36″ the emission is very faint again: here, the ionization degree varies between 0.07 and 0.23 without any definite trend. Neglecting the uncertain results for $z > 36''$, the average total density is about 1700 cm^{-3}. Assuming a mean radius of 1″, a tentative inclination angle of 25° and that the system is at a distance of 150 pc, mass loss and momentum transfer rates would be $\dot{M} = 3.8\ 10^{-8}\mathrm{M}_\odot\,\mathrm{yr}^{-1}$ and $\dot{P} = 1.6\ 10^{-5}\,\mathrm{M}_\odot\,\mathrm{yr}^{-1}\,\mathrm{km\,s}^{-1}$. This mass loss rate is two orders of magnitude larger than the value estimated by Mundt at al. (1990). The reason for this is that they used the pre-shock density calculated from n_e on the basis of planar shock models as total density, and in that way obtained n_H (pre-shock) $\sim$ 10 cm^{-3}. As stated above, the ionization in this jet could result from turbulent entrainment of ambient material, and not from

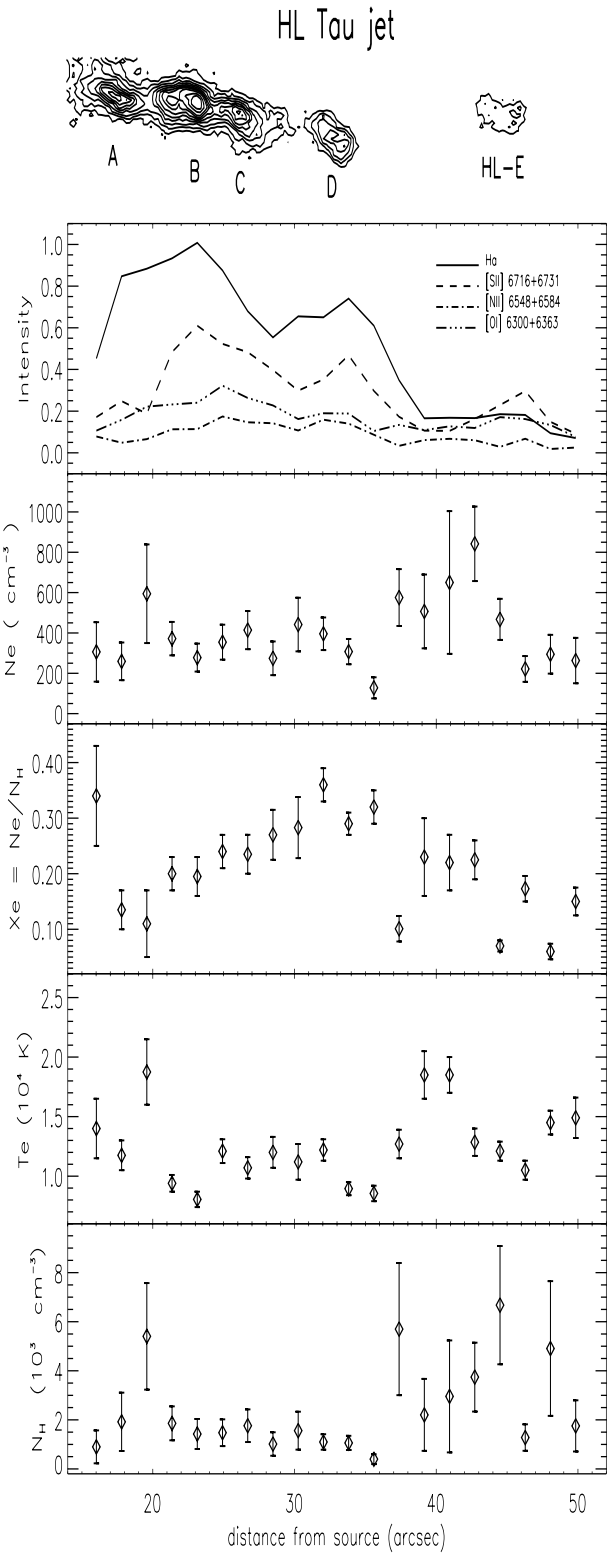

Fig. 11a–f. Physical conditions along the beam of the HL Tau jet. Distances are measured from HL Tau which was on in the long slit. The last five points refer to the HL-E knot. Panel description as in Fig. 6.

the jet properties themselves. Therefore, it seems difficult to draw firm conclusions from the results obtained for this jet.

4.6. A peculiar case: Th 28 jet (HH 228)

This flow consists of two oppositely directed jet-like structures, each about 13″ long, emanating from the unusual emission-line star Th 28, located in the Lupus T-association at a distance of about 130 pc. Several HH objects are located on both sides on the jet axis (Krautter 1986, Graham & Heyer 1988). On the western side one finds Th 28-HHW, at a distance of about 38″ from the source, while on the eastern side two regions of faint Hα emission, Th 28-HHE1 and Th 28-HHE2 are located at 30″ and 87″, respectively. The average radial velocity of the western components of the flow are $+23\,\mathrm{km\,s^{-1}}$ for the jet and +33 km s^{-1} for Th 28-HHW, while in the eastern lobe one derives $-78\,\mathrm{km\,s^{-1}}$ for the jet, $-67\,\mathrm{km\,s^{-1}}$ for HHE1, and $-87\,\mathrm{km\,s^{-1}}$ for HHE2 (Graham & Heyer, 1988). Proper motion measurements (Krautter 1986) of the HHE1 knot indicate a tangential velocity of about 320 km s^{-1}. Under the assumption that this knot is a working surface, one derives an inclination angle of this system with respect to the plane of the sky of about 10°. The spectrum of the source reveals a very active region, with many lines typical of a HH object, superposed on a strong continuum indicating the presence of an underlying star (Krautter et al. 1984).

Our analysis is limited to the western receding lobe, since the emission from the short eastern jet is heavily confused with the lines from the central region, and the knots HHE1 and HHE2 are not detectable in our spectra in the sulphur and oxygen emission lines. Furthermore, in the examined region the validity of the diagnostic is limited by the fact that the system of HH objects appears to be of high excitation. Moreover, quite unusually for HH objects, the [OI] lines are stronger than the [SII] lines over the first 4.″5 of the jet. For these reasons, the application of the diagnostic technique to this object has a qualitative character, especially for the jet section.

The electron density n_e decreases along the flow in the beam, from about 2500 cm^{-3} to about 800 cm^{-3}, and in the HH object from $\sim$ 1200 cm^{-3} to about 170 cm^{-3} (Fig. 12, panels *c*). A steep gradient of n_e along the flow was already seen by Krautter (1986). The ionization fraction in the jet appears to be rather high, except for the first position, where the [NII] emission is blended with very strong Hα; qualitatively, x_e scatters around 0.5 (left panel *d*). In knot HHW x_e decreases steadily from about 0.4 to $\sim$ 0.04 (right panel *d*). Neither in the beam section nor in the terminal knot were we able to fit the ionization data with a reliable recombination curve. The average temperature decreases from 2.5 10^4 K to 1.5 10^4 K in the jet, while it increases from about 1.3 10^4 K to 1.7 10^4 K in HHW. In the jet section the total hydrogen density decreases from about 3.3 10^4 cm^{-3} to about 1500 cm^{-3}, following the behavior of n_e; a less steep decay in n_H is derived in HHW, where it decreases from 3000 cm^{-3} to about 2500 cm^{-3}. Given the qualitative character of these results, we refrain from estimating the mass loss and momentum transfer rate for the Th 28 jet.

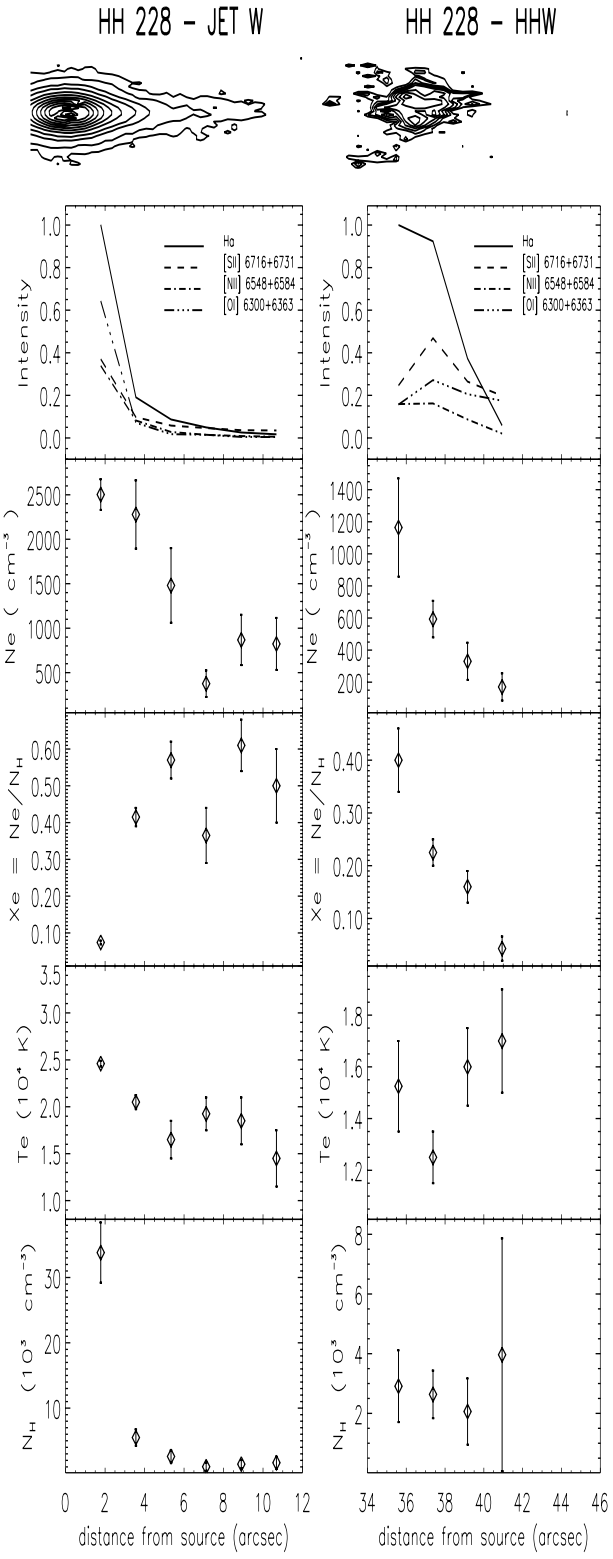

Fig. 12a–f. Physical conditions along the beam of the red lobe of the HH 228 (Th 28) jet. The left and right columns of graphs illustrate the results for the jet and for the HH object Th 28-HHW, respectively. Panels **a** are contour plots of a Hα image. The following panels are as in Fig. 6. In neither case does a reliable recombination curve fit the data points.

Table 2. Physical conditions along the beam of the examined jets

jet	selected region[b]	inclination angle[c]	opening angle	x_e range[a]	T_e range[a] (10^4 K)	n_e range[a] (10^2 cm^{-3})	n_H range[a] (10^3 cm^{-3})
HH 34	$2'' < z < 23''$	24°	$-1\overset{\circ}{.}6$	0.145–0.015	1.0–0.6	20. – 9.4–3.7	5.0–58.5–20.0
HH 46/47	$3'' < z < 45''$	28°	$1\overset{\circ}{.}0$	0.23–0.05–0.1	1.6–2.2–0.9	12.0–1.1	4.3–16.9 – $\sim$ 3.0
HH 24C	$14'' < z < 22''$	25°	$-2\overset{\circ}{.}0$	0.24–0.26	2.0–1.1	6.3–8.8–4.9	2.6–3.8–1.9
	$23'' < z < 35''$	25°	$1\overset{\circ}{.}0$	0.34 – $\sim$0.2	1.1–2.0–1.0	3.2–4.7–1.8	1.0–3.7–0.6
	$-2'' > z > -9''$	25°	$2\overset{\circ}{.}0$	0.15–0.06	1.2–1.5–0.8	$\sim$14.0–6.0	8.0–23.0–12.0
HH 24E	$-10'' > z > -20''$	25°	$0\overset{\circ}{.}0$	0.36–0.19	1.0–1.1–0.5	$\sim$5.6 – $\sim$2.0	$\sim$3.5–0.7–1.7
	$-21'' > z > -29''$	10°	$1\overset{\circ}{.}0$	0.38–0.3	1.0–1.2	$\sim$7.0 – $\sim$14.0	2.1–4.2
	$37'' < z < 52''$	30°	$2\overset{\circ}{.}0$	$\sim$0.2 – $\sim$0.1	1.0–0.8–1.1	3.5–0.8–3.5	$\sim$2.0–0.7 – $\sim$3.3
HH 24G	$53'' < z < 63''$	30°	$-10\overset{\circ}{.}0$	0.22 – $\sim$0.18	1.1–0.8	1.3–4.0–3.5	0.6–2.3–1.5
	$64'' < z < 66''$	30°	$20\overset{\circ}{.}0$	0.31–0.26	1.08–1.12	6.0–5.5	1.7–2.1
HL Tau	$18'' < z < 36''$	–	–	0.14–0.36	1.2–1.9 – 0.9	2.5–6.0–1.0	1.9–5.4–0.4
HL Tau/HL-E	$43'' < z < 50''$	–	–	0.06–0.17	1.1–1.5	4.6-2.0	$\sim$6.7 – $\sim$2.0
Th 28 - jet[d]	$2'' < z < 11''$	12°	–	0.07–0.61	2.4–1.4	25. – 4.0–8.2	33.0–1.0–1.6
Th 28 - HHW	$35'' < z < 41''$	$\sim 10^\circ$	–	0.40–0.04	1.3–1.7	11.6–1.7	2.9–3.9

[a] Approximate limiting values from the beginning to the end of the indicated region. An intermediate value refers to a localized peak or a marked decay in the selected region. See the plots for details.
[b] Projected distance from the source.
[c] The inclination angles for HH 34, HH 46/47 and Th 28 are from Eislöffel & Mundt 1992, Eislöffel & Mundt 1994, and Krautter 1986, respectively. The values for the other jets are estimated from our recombination model.
[d] Red lobe.

5. General discussion

We would like to emphasize once more that our results on jet ionization fraction and average excitation temperature do not depend on a model of the heating mechanism and/or the jet evolution. On the other hand, restrictions of our analysis should also be pointed out. First, our sample is rather small, so that individual characteristics of the examined objects may somewhat limit our ability to derive generalized properties of HH jets. Secondly, it should be kept in mind that our spatial resolution usually is insufficient to resolve single knots. Also, the use of line ratios from intensities integrated over the full line width does not allow to disentangle contributions from different velocity components of the jet. Therefore, the result for each position along the beam is an average over a relatively large parcel of gas, which could contain regions of very different conditions, e.g. near an unresolved shock front. This affects especially our derived temperatures, which only roughly indicate the average excitation temperature of the forbidden lines. Thirdly, the technique is capable of identifying regions of high ionization, but there the application of the procedure may become critical due to the neglect of photoionization in the regulation of the ionization state of O and N (see Sect. 3.1). Therefore, if a value of $x_e > 0.6$ is obtained, the result should be taken with caution.

Despite these difficulties the application of our technique to spatially resolved spectra of 'classical' Herbig-Haro jets gives us a number of interesting insights into the physics of these objects, which we discuss in the following.

5.1. Ionization in HH jets

For all examined objects, the gas in the beams turns out to be *partially ionized*. In Table 2 we summarize the values of x_e derived in each jet, together with the average temperatures, and the electron and total hydrogen densities. In most cases the hydrogen ionization fraction ranges between 0.02 and 0.35. It is generally lower for less excited and heavier jets, and higher for more excited and lighter ones. Qualitatively, the ionization fraction is also higher on average in regions where the jet beam violently interacts with its surroundings, as in the faint section of the HH 46/47 beam. Of the jets studied, the least ionized appears to be HH 34 ($x_e \sim 0.03$ in the bright beam), which also presents the highest [SII]/Hα ratio and the highest densities.

The ionization degrees we find in our objects are generally higher than those diagnosed by HMR94. These authors derive the hydrogen ionization fraction comparing observed line ratios with a grid of planar shock models, varying the pre-shock density, shock speed, and parallel magnetic field. The extremely low ionization fraction in these models comes as a natural consequence of the fact that the observed ratios should be produced by low excitation (i.e. low velocity) shocks, ranging from 20 to 40 km s^{-1}. As HMR94 illustrate in their Fig. 1, a 35 km s^{-1} shock propagating in a neutral medium with pre-shock density $n \sim 10^3$ cm^{-3} is not able to produce *in situ* an ionization fraction greater then $x_e \sim 0.03$. It is worth noting, however, that the average ionization given by HMR94 is highly influenced by the results from line ratios involving Balmer lines, like [OI]/Hα, [SII]/Hα, [NII]/Hβ, that lead systematically to ionization frac-

Table 3. Average mass loss and momentum transfer rates

jet	distance (pc)	radius ($''$)	space velocity ($km\,s^{-1}$)	average n_H ($10^3\,cm^{-3}$)	$\dot{M}$ ($M_\odot\,yr^{-1}$)	$\dot{P}$ jet ($M_\odot\,yr^{-1} \times km\,s^{-1}$)	$\dot{P}$ mol. flow[a] ($M_\odot\,yr^{-1} \times km\,s^{-1}$)	reference[b]
HH 34	480	0.4	220	20.0	$3.7\,10^{-7}$	$8.1\,10^{-5}$	$2.0\,10^{-7}$	1,2,3,4,5,6
HH 46/47[c]	450	0.4	300	4.3	$9.4\,10^{-8}$	$2.8\,10^{-5}$	$1.0\,10^{-4}$	1,6,7,8,9,10
HH 24C	480	0.55	425[d]	2.1	$1.4\,10^{-7}$	$6.0\,10^{-5}$	–	1,11,12
HH 24E	480	0.35	355[d]	5.6	$1.3\,10^{-7}$	$4.5\,10^{-5}$	–	1,11,12
HH 24G	480	2.5	260[e]	1.4	$1.2\,10^{-6}$	$3.1\,10^{-4}$	–	1,11,12
HL Tau[f]	150	1	425[d]	1.7	$3.8\,10^{-8}$	$1.6\,10^{-5}$	$6.6\,10^{-6}$	1,13,14,15,16

[a] blueshifted lobe

[b] 1 = this paper; 2 = Eislöffel & Mundt 1992; 3 = Heathcote & Reipurth 1992; 4 = Raga et al. 1991; 5 = Ray et al. 1996; 6 = Chernin & Masson 1995; 7 = Eislöffel & Mundt 1994; 8 = Heathcote et al. 1996; 9 = Chernin & Masson, 1991; 10 = Olberg et al. 1992; 11 = MRR91; 12 = Eislöffel & Mundt 1997; 13 = Mundt et al. 1990; 14 = Lopéz et al. 1995; 15 = Cabrit et al. 1996; 16 = Monin et al. 1996

[c] selected region: $3'' < z < 45''$ from the source.

[d] for an inclination angle to the plane of the sky of 25°.

[e] assuming an inclination angle to the plane of the sky of 30°.

[f] selected region: $18'' < z < 36''$ from HL Tau.

tions a factor 2 lower than those derived from [NII]/[OI] and [NI]/[NII] (see their Table 3). The authors interpret this discrepancy as arising from the simplyfying assumption of planar shock geometry. On the other hand, the $< x_e >$ values derived in HMR94 from the [NII]/[OI] ratio are very close to the ones we find from analogous observational data. Since the [NII]/[OI] ratio is extremely sensitive to the ambient ionization (see the orientation of our [OI]/[NII] curve in Figs. 4 and 5), one might ask if HMR94 possibly underestimate the average ionization using line ratios involving Balmer lines. This can occur if processes other than shock excitation at a fixed temperature suppress Hα in comparison with forbidden lines. In this case, the use of the curves in Figs. 3, 4 and 5 of HMR94, that provide $< x_e >$ as a function of [SII]/Hα, [OI]/Hα, [NII]/Hβ would lead to exceedingly low ionization fractions (and shock speeds). Such a situation may arise if the shock propagates in an already ionized medium. A pre-ionization would reduce the number of neutral H atoms available to produce collisionally excited Hα at a given temperature. An additional ionization would increase also the amount of the recombination contribution, but for weak shocks this would be minor in comparison with collisional Hα (see Fig. 14 of HMR94), unless the pre-ionization is substantial. As a consequence, in jets like the ones examined by HMR94, where the ionization is moderate, one would underestimate $< x_e >$ using ratios involving Balmer lines.

The necessity of taking the pre-ionization history of the gas into account is suggested by the fact that in most of our observed jets the ionization fraction slowly decreases along the jet or at least sections of it. This is in accord with the idea of slow time dependent recombination along the beam suggested by BCO95: since the typical recombination time of the jet gas is of the order of the travel time through the bright jet section, partially ionized material can still be observed at large distances from the source if the jet gas gets almost completely ionized in the acceleration region. In their model the initial ionization is produced by a violent shock which is heavily shielded from view by circumstellar material. The ionization state soon decouples from the local thermodynamic conditions due to the sudden expansion of the jet beam (such a rapid expansion has been suggested, for example, in MRR91); the jet recollimates and the ionization fraction gently decreases along the jet axis on spatial scales determined by the product of recombination time and the flow velocity. This scenario is not necessarily in contradiction with the presence of shocks in the flow if these are too weak to produce further ionization. Jet shock calculations, however, should take the fact into account that the fronts may form in a medium that already has a considerable ionization degree.

In order to test the BCO95 recombination model, we calculated recombination curves, and superimposed them on the ionization data. Our model, described in more detail in the Appendix, assumes that the jet gas flows along surfaces shaped as nested cones that diverge or converge monotonically over a finite length. We point out that by taking the average flow radius, flow speed, and electron density from optical images, we implicitly assume that the average properties of the flow are those of the zones of maximum emission, which in turn are those of maximum compression (see Sect. 5.3 for a discussion). The curves are calculated by varying the opening angle of the flow until the best fit is obtained. In HH 34 and in the bright section of HH 46/47 the overall behavior can be described by a single family of self-similar cones. In HH 24C, HH 24E and HH 24G, however, marked jumps in the ionization degree, each followed by a well defined independent decay are seen. The ionization fraction in these jets is best reproduced by a series of independent flow cones of different opening angles (see below). With the exception of the HH 24G flow, which shows a diffuse appearance, the resulting best-fit opening (positive or negative) angles are small, scattering around values of a few degrees. This is in good agreement with the results of MRR91, who measured the apparent flow diameters on optical images (which might not be the actual dynamical flow surfaces, if cold, unobservable gas was moving at the true boundary of the flow). Our estimates,

on the other hand, come from a fluid model, albeit assuming an initial jet diameter based on observations. The agreement between the two opening angles is not fortuitous if one considers that inertia alone provides a free-flowing opening angle of at most a few degrees for a Mach 20–30 jet.

A plausible interpretation for the jumps in the ionization fraction in the HH 24C/E/G jets seems to be the presence of shocks strong enough to reionize the gas in the beam. The [OI]/[NII] ratio invariably presents a minimum in these positions. Moreover, the subsequent smooth decay of the ionization fraction always occurs *downstream of the jump* in the HH 24C/E/G jets. This is in apparent conflict with a bow shock interpretation of these knots: a bow shock would produce a jump in the ionization degree with a decay upstream of the jump. If a Mach disk strong enough to ionize the gas was associated with the bow shock, the ionization fraction should increase at the location of that Mach disk, then decrease inside the working surface, and peak again at the front shock (such a feature is indeed observed inside HH 47A (see Fig. 7)). At our spatial resolution, we may not be able to resolve this structure in an internal bow shock. Instead, we would only observe a jump in $x_{\rm e}$ moving along the beam at about the jet speed. The fact that the ionization fraction decreases downstream of the jump is consistent with the flow passing a throat that compresses it. An oblique shock may form there, capable of reionizing the gas. Downstream of the shock the jet material then progressively looses its ionization.

While the shape of the ionization decay clearly indicates that most of the knots in our jet beams do not show the behavior expected for mini-bow shocks, this investigation alone may not be sufficient to discard the formation of such internal working surfaces. It seems possible that the interaction of the central beam with the surrounding medium comes into play. It is clear from HST images that the high ionization of the faint section in the HH 46/47 flow is due to the formation of shocks along the boundary of the wiggling flow, which also propagate in the surrounding medium. On the other hand, the jumps in HH 24E and HH 24G probably are better interpreted as the interaction between the jet beam and dense clumps in the medium. The shocks disturbing the beam may be generated when the jet collides with and/or perforates one of these dense clumps. The comprehension of this phenomenon would be greatly improved by proper motion measurements of the individual condensations. This could help disentangling if the knots are actually associated with steady nebular clumps or if they are nearly comoving with the jet: in the latter case the excitation of the beam gas could be related to the nonlinear development of Kelvin-Helmholtz instabilities arising in the interaction with a comoving jet cocoon.

5.2. Temperature

Apart from the ionization fraction, our diagnostic diagrams indicate an average excitation temperature. We generally find values of about 9000 to 12000 K, with minima and maxima of about 5000 and 24000 K in isolated positions. If the knots do represent shocks, even if weak, the temperature actually rises after the shock front well above these values and then decreases rapidly up to two orders of magnitude in the post shock cooling region. We are unable to observe such features here, since the typical length of a post-shock cooling layer (10–100 AU) is much smaller than our spatial resolution, which for example at the distance of HH 34 corresponds to $\sim 1.2\ 10^{16}$ cm. Therefore, even if weak shocks are present in the flow we measure only an average temperature of the emission regions of the considered forbidden lines. Taking this into account, the results of our diagnostic are not in conflict with the results of shock calculations. The application of our technique to data of much higher spatial resolution could in principle allow us to retrieve the temperature variations predicted by shock models in the forbidden line emission region. Although at the present resolution our temperatures have only a limited physical meaning, we note that they can nevertheless give a qualitative information concerning the characteristics of the shocks exciting the gas. In fact, where a moderate to high ionization fraction is observed simultaneously with a low temperature, either a relatively high velocity of the shock, or a shock front forming in a region of high pre-ionization are indicated.

5.3. Total jet density

One of the main goals of this work was the determination of the total jet density. The total hydrogen density $n_{\rm H}$ calculated from $n_{\rm H} = n_{\rm e}/x_{\rm e}$ ranges between about 10^3 cm^{-3} and a few 10^4 cm^{-3} for a heavier jet like HH 34. Due to our limited spatial resolution we can only derive average densities over large parcels of gas, and we may ask ourselves if we under- or overestimate the total density, and if a correction factor should be applied as in HMR94. These authors suggest that any determination of $n_{\rm H}$ involving line ratios from post-shock cooling layers should take into account the compression of the emitting gas. Thus, in order to determine the average density, they take a geometric mean of the pre-shock and post-shock values. This in turn involves the multiplication of the $n_{\rm H}$ determined by line diagnostics by a factor C$^{-1/2}$, where C is the shock compression defined as the ratio between the post- and pre-shock densities averaged over the [SII] emission region. That way, they find the densities in the HH 34 and HH 47 jets lower than those directly determined as the ratio $n_{\rm e}/x_{\rm e}$ by a factor 1/4 and 1/5, respectively. HMR94 also observe that $n_{\rm H}$ determinations from the observed luminosity in a suitable forbidden line, like [OI]λ 6300, should not be corrected for compression, since even if the emission comes from the densest part of the flow, it is diluted over the observing aperture, which tends to cancel the estimate error.

Since our results come from line ratios, filling factor effects are unimportant. On the other hand, our derived values are also weighted strongly towards regions of maximum emission, which in turn are those of maximum compression. In this respect our values may overestimate the average density, too. If shock excitation is responsible for the heating of the gas, we should apply a correction factor as well. This may also be suggested by the fact that including shock compression HMR94 find mass

loss rates almost identical to those provided by the luminosity in the [OI] line, while ours turn out to be larger. However, since our results do not derive from a shock model, there are large uncertainties associated with the adoption of correction factors. Thus, we prefer here to give total densities as direct ratios between the electron density and the ionization fraction. It should be kept in mind that while $x_{\rm e}$ determinations are unaffected by shock compression, both the electron and the total density might be overestimated, possibly by a factor 3 to 5. A comparison between the jet surface brightness predicted by our results and refined spectrophotometric measurements will help clarifying this aspect in the future.

5.4. Jet mass loss and momentum transfer rates

In Table 3, we summarize the derived values for the mass loss and momentum supply rates in the examined jets, under the assumption that the density is constant over the jet section, and equal to the average over the indicated region. Since we do not apply a correction factor for shock compression, $\dot{M}$ and $\dot{P}$ may be overestimated by the same factor as the derived densities. Also, the estimate of $\dot{M}$ and $\dot{P}$ is highly dependent on the flow radius and the assumed spatial jet velocity, which is not always known since the inclination angle of the jet axis is not known. We find the average mass loss rate to vary from 3.8 10^{-8} (HL Tau jet) to 1.2 $10^{-6}\,{\rm M}_\odot\,{\rm yr}^{-1}$ (HH24 G), while momentum transfer rates vary between 1.6 10^{-5} (HL Tau jet) and 3.1 $10^{-4}\,{\rm M}_\odot\,{\rm yr}^{-1}\,{\rm km\,s}^{-1}$ (HH 24G). In three of our objects a molecular outflow is known to be associated with the optical jets, and it is interesting to compare the corresponding momentum transfer rates. For the HH 34 jet, we find $\dot{P} = 8.1\ 10^{-5}\,{\rm M}_\odot\,{\rm yr}^{-1}\,{\rm km\,s}^{-1}$, while Chernin & Masson (1995) find $\dot{P} \sim 2.0\ 10^{-7}\,{\rm M}_\odot\,{\rm yr}^{-1}\,{\rm km\,s}^{-1}$ for the weak blue lobe of the molecular outflow, assuming a dynamical time of 10^4 yr. For the HL Tau jet $\dot{P} = 1.6\ 10^{-5}\,{\rm M}_\odot\,{\rm yr}^{-1}\,{\rm km\,s}^{-1}$ (assuming an inclination angle of 25°), while for the blueshifted part of the associated molecular outflow Monin et al. (1996) derive $\dot{P} = 6.6\ 10^{-6}\,{\rm M}_\odot\,{\rm yr}^{-1}\,{\rm km\,s}^{-1}$. These results suggest that the jets supply enough momentum per unit time to drive the surrounding molecular flow. In HH 46/47, however, the blue lobe of the molecular outflow possesses a momentum transfer rate of $1\ 10^{-4}\,{\rm M}_\odot\,{\rm yr}^{-1}\,{\rm km\,s}^{-1}$ (Chernin & Masson 1991, 1995), while we find a lower value, $\dot{P} = 2.8\ 10^{-5}\,{\rm M}_\odot\,{\rm yr}^{-1}\,{\rm km\,s}^{-1}$ for the jet, even without correcting for shock compression.

5.5. Further consequences for jet models

We already mentioned the importance of taking partial ionization into account in reliable shock models of the internal beam excitation. Moreover, partial ionization may introduce important differences in the modelling of magnetic acceleration and collimation of jets. When a substantial fraction of neutrals is present, ambipolar diffusion and other drift effects must be taken into account, introducing additional terms to the usual set of magnetohydrodynamic equations. Bacciotti et al. (1997) suggest that in a plasma with 10% ionization a term corresponding to the Hall effect should be introduced in the magnetic induction equation. The dispersive nature of this term leads to a weakening of the shocks that may eventually form in the beam.

6. Conclusions

In this paper we investigated the physical conditions in the beams of a number of well-known Herbig-Haro jets, using a diagnostic technique that allows one to derive the ionization fraction of the emitting gas directly from the observed spectra. The procedure uses ratios of the most commonly observed forbidden lines in HH jets, and is based on the fact that in the jet beam the ionization state of O and N can be assumed to be related to the ionization fraction of hydrogen through charge exchange (which is dominant), collisional ionization and radiative plus dielectronic recombination. We carefully checked our procedure to be consistent with the results of shock calculations, as those presented in HMR94, and find our results in good agreement. Here, we present the results for a sample of optical outflows, namely: HH 34, HH 46/47, HH 24G, HH 24C/E, HL Tau and HH 228 (Th 28). They can be summarized as follows.

1 – For all examined objects the gas in the beam is *partially ionized*; the hydrogen ionization fraction $x_{\rm e}$ typically ranges between 0.02 and 0.35, being higher for more excited and lighter jets. The diagnostic also indicates qualitatively that in regions of violent interaction between the beam and its surroundings, the ionization degree can be much higher, as in the faint section of the HH 46/47 jet.

2 – With the exception of the HL Tau jet *the ionization fraction is generally observed to slowly decrease along the jet or along sections of it*. As originally suggested by BCO95, the ionization state of the jet gas is probably produced in the acceleration region; then the gas slowly recombines traveling away from the source on temporal scales comparable to the travel time through the bright section of the jet. The HH 34 jet and the first section of the HH 46/47 jet are described by a single recombination curve of a conical flow model: here, internal shocks are likely to be too weak to appreciably contribute to the ionization. On the contrary, the HH 24E/C/G outflows show evidence of re-ionization events, and are better described by a series of recombination curves of different opening angles. We find best-fitting curves corresponding to opening angles of only a few degrees for most objects, in good agreement with the results of MRR91, and derive first estimates of the inclination angle for some flows. In the HL Tau jet the ionization fraction is observed to steadily increase along the flow. Here, however, $x_{\rm e}$ could be 'pumped' by a turbulent boundary layer, whose presence has been suggested on the basis of the Hα line profile.

3 – Where re-ionization episodes are present, *the decay in $x_{\rm e}$ is always observed downstream of the ionization jump*. This raises new questions about the nature of shocks exciting the beam gas, because it contradicts the current paradigm which interprets the jet knots as internal bow shocks. The observed downstream decrease is more consistent with the flow passing through a shock front produced by, for example, Kelvin-Helmholtz instabilities

arising in the interaction between the beam and its surrounding cocoon, or alternatively, when the jet collides with local nebular clumps. Bow shocks may be present as well in the jet beams, but they are required to be too weak to substantially alter the ionization state of the flowing gas.

4 – The average excitation temperature varies typically between 9000 and 12000 K. The limited spatial resolution of the investigated spectra does not allow us to study the post-shock cooling region in detail: the temperatures we derive are only a rough indication of the average excitation temperature of the forbidden lines emission region; taking this constraint into account, our results are not in contradiction with the prediction of radiative shock models (HMR94).

5 – The average total hydrogen density $n_{\rm H} = n_{\rm e}/x_{\rm e}$ ranges between about 10^3 and a few 10^4 cm^{-3}. Because of the difficulties to derive the shock compression factors, we do not attempt any correction to the derived values. This may lead to overestimates of the flow density, by a factor 3–5. Average mass loss and momentum transfer rates calculated under the assumption of constant density over the jet section are summarized in Table 3. We find that the momentum supply rates of the HH 34 jet and possibly of the HL Tau jet are large enough to drive their molecular outflows. This may not be the case for HH 46/47, where our estimate yields a momentum transfer rate of the optical jet less than one third of that associated with the molecular outflow.

6 – Our findings confirm that partial ionization is a dominant characteristic of the beams of HH jets, and we stress the importance of taking it into account in any jet model. Reliable calculations for beam shocks should consider that the fronts advance in a medium which could be already substantially ionized. This would greatly influence the cooling properties of the flow and the model predictions concerning line emission. In addition, partial ionization may introduce important differences in the modeling of magnetized jets, due to the effects introduced by collisions between charged particles and neutrals.

Acknowledgements. We thank Reinhard Mundt for sharing spectra with us. We are grateful to Pat Hartigan for his calculations and valuable criticism of an earlier version of the manuscript, and to Tom Ray, Sergei Lamzin and J.A. Rodriguez-Gasper for useful comments and suggestions.

Appendix: calculation of the recombination curves

In the absence of energetic radiative sources and assuming that local collisional processes are too weak to produce substantial hydrogen ionization the equation governing the decoupled time-dependent recombination of the gas can be easily found combining the standard continuity equations for the total and electron densities (see, e.g., Osterbrock 1989) through $x_{\rm e} = n_{\rm e}/n_{\rm H}$. The final equation for the ionization fraction in this simple case reads:

$$\frac{Dx_{\rm e}}{Dt} = -n_{\rm H} x_{\rm e}^2 \alpha_B(H^0, T) \qquad (2)$$

where $D/Dt = \partial/\partial t + \mathbf{v}\cdot\nabla$ is the substantial time derivative, with $\mathbf{v}$ the flow speed, and $\alpha_B(H^0, T)$ is the recombination coefficient valid in Case B (Hummer & Storey 1987).

We assume that in the recollimated portion of the jet the gas flows on average along a set of axisymmetric nested flow surfaces, which in a cylindrical coordinate system and in the proper frame of the source are described by the equations $r(\zeta) = \xi R_{\rm j}(\zeta)$, where ζ is the axial coordinate, and $R_{\rm j}(\zeta)$ is the local radius of the jet channel. The parameter ξ labels the different surfaces, the axis being identified by $\xi = 0$ and the external boundary of the jet, by $\xi = 1$. We neglect azimuthal motions, and take a constant value of the axial velocity v_ζ all over the flow. Variations of the quantities with time can therefore be described as variations along the spatial coordinate ζ. It is easily shown that in these conditions the total density of a fluid particle behaves as: $n_{\rm H}(r,\zeta) = n_{\rm H}(r,\zeta_0) R_{\rm j}^2(\zeta_0)/R_{\rm j}^2(\zeta)$, where $n_{\rm H}(r,\zeta_0)$ and $R_{\rm j}(\zeta_0)$ are the hydrogen density and the channel radius at the arbitrarily chosen initial point of the integration ζ_0. Here we will assume for simplicity that the flow surfaces are shaped as nested cones, so that $R_{\rm j}(\zeta) = R_{\rm j}(\zeta_0) + \tan(\theta)(\zeta - \zeta_0)$, where θ is the average opening angle of the jet (which is positive for diverging jets and negative for converging ones). Coherently with the spectral read-out we adopted, we shall limit ourselves to the study of the fluid particles located on the axis of the flow, assigning to each of them the average physical properties of the jet section the particle belongs to.

Under these assumptions, and expressing variables and coordinates through quantities directly related to observations, the solution of equation (2) can be written as:

$$x_{\rm e}(z) = x_{\rm e}(z_0)\frac{1 + f(z - z_0)}{1 + (g + f)(z - z_0)} \qquad (3)$$

where z is the axial distance from the source projected on the plane of the sky and expressed in arcseconds, z_0 is the starting point of the integration, that in practice is the first position along the beam for which a determination of the ionization fraction is available, or the position of an ionization jump (see e.g. Figs. 8, 9, 10). In expression (3) the quantities f and g are defined as follows:

$$f = \frac{\tan\theta}{\cos i \cdot R_{\rm a}(z_0)}$$

$$g = 0.149\ \tan i \cdot \left(\frac{n_{\rm e}(z_0)}{10^2\ {\rm cm}^{-3}}\right) \cdot \left(\frac{\alpha(H^0,T)}{10^{-13}\ {\rm cm}^3\ {\rm s}^{-1}}\right) \cdot \cdot \left(\frac{10^5\ {\rm cm\ s}^{-1}}{v_{\rm rad}}\right) \cdot \left(\frac{D}{10^2\ {\rm pc}}\right)$$

where i is the inclination angle of the beam with respect to the plane of the sky, $R_{\rm a}$ is the jet radius expressed in arcseconds, D is the distance to the object in parsecs, and $v_{\rm rad}$ the observed line of sight velocity of the emitting gas in the jet. The free parameters are the opening angle θ, which is varied until the best fit is obtained, and the inclination angle i of the jet to the plane of the sky, if not known independently. It should be kept in mind that in the framework of this simple model the jet is

assumed to diverge or converge monotonically over its entire length or over separate portions of the flow: the jet radius to which we refer is, however, that corresponding to the zones of maximum emission, which in turn are the zones of maximum compression. The curves, therefore, refer to average properties of the flow, weighted more by the brightest regions.

References

Arnaud M., Rothenflug R., 1985, A&AS 60, 425
Bacciotti F., Chiuderi C., Oliva E., 1995, A&A 296, 185 (BCO95)
Bacciotti F., Hirth G., Natta A., 1996, A&A 310, 309 (BHN96)
Bacciotti F., Chiuderi C., Pouquet A., 1997, ApJ 478, 594
Bodo G., Massaglia S., Ferrari A., Trussoni E., 1994, A&A 283, 655
Bührke T., Mundt R., Ray T.P., 1988, A&A 200, 99
Chernin L.M., Masson C.R., 1991, ApJ 382, L93
Chernin L.M., Masson C.R., 1995, ApJ 443, 181
Cabrit S., Edwards S., Strom S., Strom K., 1990, ApJ 354, 687
Cabrit S., Guilloteau S., Andrè P., et al., 1996, A&A 305, 527
Edwards S., Cabrit S., Strom S., et al., 1987, ApJ 321, 473
Eislöffel J., 1996 In: W. Kundt (ed.) Jets from Stars and Galactic Nuclei. Lecture Notes in Physics vol. 471, 104
Eislöffel J., Mundt R., 1992, A&A 263, 292
Eislöffel J., Mundt R., 1994, A&A 284, 530
Eislöffel J., Mundt R., 1997, AJ 114, 280
Falle S.A.E.G., Raga A.C., 1993, MNRAS 261, 573
Falle S.A.E.G., Raga A.C., 1995, MNRAS 272, 785
Graham J.A., Heyer M.H., 1988, PASP 100, 1529
Hardee P.E., Stone J.M., 1997, ApJ 483, 121
Hartigan P., Morse J.A., Raymond J., 1994, ApJ 436, 125 (HMR94)
Heathcote S.R., Reipurth B., 1992, AJ 104, 2193
Heathcote S.R., Morse J.A., Hartigan P., et al., 1996, AJ 112, 1141
Hummer D.G., Storey P.J., 1987, MNRAS 224, 801
Kingdon J.B., Ferland G.J., 1996, ApJS 106, 205
Krautter J., 1986, A&A 161, 195
Krautter J., Reipurth B., Eichendorf W., 1984, A&A 133, 169
Landini M., Monsignori-Fossi B., 1990, A&AS 82, 229
Lopéz R., Raga A.C., Riera A., Anglada G., Estalella R., 1995, MNRAS 274, L19
Monin J.L., Pudritz R.E., Lazareff B., 1996, A&A 305, 572
Morse J.A., Hartigan P., Heathcote S., Raymond J.C., Cecil G., 1994, ApJ 425, 738
Mundt R., Fried J.W., 1983, ApJ 274, L83
Mundt R., Ray T.P., Bührke T., Raga A.C., Solf J., 1990, A&A 232, 37
Mundt R., Ray T.P., Raga A.C., 1991, A&A 252, 740 (MRR91)
Nussbaumer H., Storey P.J., 1983, A&A 126, 75
Olberg M., Reipurth B., Booth R., 1992, A&A 259, 252
Osterbrock D.E., 1989, Astrophysics of Gaseous Nebulae and Active Galactic Nuclei. University Science Books, Mill Valley, CA
Raga A.C., 1991, AJ 101, 1472
Raga A.C., Mundt R., Ray T.P., 1991, A&A 252, 733
Raga A.C., Mellema G., Lundqvist P., 1997, ApJ 109, 517
Ray T.P., 1996, In: Tsinganos K. (ed.) Solar and Astrophysical MHD Flows. Kluwer Academic Publishers, p. 539
Ray T.P., Mundt R., Dyson J.E., Falle S.A.E.G., Raga A.C., 1996, ApJ 468, L103
Reipurth B., Bally J., Graham J.A., Lane A.P., Zealey W.J., 1986, A&A 164, 51
Reipurth B., Hartigan P., Heathcote S., Morse J., Bally J., 1997, AJ 114, 757
Savage B.D., Mathis J.S., 1979, ARA&A 17, 73
Solf J., 1987, A&A 184, 322
Stone J.M., Norman M.L., 1993, ApJ 413, 210
Stone J.M., Xu J., Hardee P.E, 1997, ApJ 483, 136
Strom K.M., Strom S.E., Vrba F.J., 1976, AJ 81, 308